REPORT DOCUMENTATION PAGE

AFRL-SR-AR-TR-03-

0404

1. REPORT DATE (DD-MM-YYYY)	2. REPORT TYPE	3. DATES COVERED
September 12, 2003	Final Report	200/09/01 - 2002/08/31

4. TITLE AND SUBTITLE
Laboratory-Based Atmospheric Turbulence Experiments: C2 - Characterization and Non-Kolmogorov Propagation

5a. CONTRACT NUMBER
F49620-00-1-0343

5b. GRANT NUMBER

5c. PROGRAM ELEMENT NUMBER

6. AUTHOR(S)
Dr. Ron Hugo

5d. PROJECT NUMBER

5e. TASK NUMBER

5f. WORK UNIT NUMBER

7. PERFORMING ORGANIZATION NAME(S) AND ADDRESS(ES)

University of Calgary
ES 602 Research Services
2500 University Drive NW
Calgary, AB T2N 1N4

8. PERFORMING ORGANIZATION REPORT NUMBER

9. SPONSORING / MONITORING AGENCY NAME(S) AND ADDRESS(ES)
Air Force Office of Scientific Research
801 N. Randolph Street
Room 732
Arlington, VA 22203
FAX: (703) 696-8450

10. SPONSOR/MONITOR'S ACRONYM(S)
AFOSR/NM

11. SPONSOR/MONITOR'S REPORT NUMBER(S)

12. DISTRIBUTION / AVAILABILITY STATEMENT
Approved for public release, distribution unlimited

20031028 203

13. SUPPLEMENTARY NOTES

14. ABSTRACT
Fluid-mechanic and optical-based measurements have been used to examine the nature of turbulence statistics in a heated axisymmetric jet. Single-component streamwise velocity fluctuation spectra have indicated the flow to have a -5/3 spectral slope within 7 jet diameters of the jet's exit. Structure functions computed using both angle of arrival and optical phase were found to be inconclusive at identifying non-Kolmogorov statistics within the jet. Spectral slopes of angle-of-arrival signals were found to be useful at indicating anisotropy in the optical turbulence in a region that appeared Kolmogorov using single-component fluid mechanic measurements. Subsequent two-component velocity measurements have verified the optically-detected flow anisotropy. Anisotropy occurs in flow regions where there are large differences between longitudinal and lateral velocity components. Both fluid-mechanic and optical statistics collected along the major flow axis (longitudinal direction) have Kolmogorov statistics, while data collected in directions transverse to the major flow axis (lateral direction) have non-Kolmogorov statistics.

15. SUBJECT TERMS

16. SECURITY CLASSIFICATION OF:			17. LIMITATION OF ABSTRACT	18. NUMBER OF PAGES	19a. NAME OF RESPONSIBLE PERSON
a. REPORT	b. ABSTRACT	c. THIS PAGE		59	19b. TELEPHONE NUMBER (include area code)

FINAL REPORT TO THE
AIR FORCE OFFICE OF SCIENTIFIC RESEARCH
FOR THE PROJECT

LABORATORY-BASED ATMOSPHERIC TURBULENCE EXPERIMENTS: C_n^2 - ϵ CHARACTERIZATION AND NON-KOLMOGOROV PROPAGATION

Submitted by

RONALD J. HUGO (PI)
Department of Mechanical and Manufacturing Engineering
The University of Calgary

Grant No. F49620-00-1-0343

UNIVERSITY OF CALGARY
2500 University Dr NW
Calgary, Alberta, Canada
T2N 1N4

Contents

1. STATUS OF EFFORT

Research has been conducted investigating non-Kolmogorov turbulence statistics in a heated axisymmetric jet. Both fluid-mechanic and optical-based measurements have been used to examine the nature of turbulence statistics in the heated axisymmetric jet. Fluid-mechanic measurements consisting of mean velocity, mean temperature, fluctuating velocity, and fluctuating temperature have been made. Optical measurements consisting of one-dimensional optical phase and angle-of-arrival have been made. The jet flow has been investigated at locations ranging from one to twenty nozzle diameters downstream of the jet exit plane.

The jet provides a flowfield that is time invariant, accessible to both fluid mechanic and optical measurements, and has non-Kolmogorov turbulence statistics. The utility of this investigation to USAF programs is that the fluid-mechanic statistics, consisting of velocity and temperature fluctuation data, is representative of a large amount of data that has been collected by AFRL/DEBA during atmospheric turbulence characterization experiments. The AFRL data, collected using both balloon and aircraft, has been made using fluid-mechanic-based measurements and assumes atmospheric turbulence to have Kolmogorov statistics (isotropic and homogeneous). The fluid-mechanic-based data collected by AFRL/DEBA has been related to optical turbulence statistics and used to predict the performance of optical systems.

Single-component streamwise velocity fluctuation spectra have indicated the flow to have a -5/3 spectral slope within 7 jet diameters of the jet's exit. Structure functions computed using both angle of arrival and optical phase were found to be inconclusive at identifying non-Kolmogorov statistics within the jet. Spectral slopes of angle-of-arrival signals were found to be more useful at indicating anisotropy in the optical turbulence, with power-law dependencies of $f^{-2/3}$ for Kolmogorov statistics and f^{-1} for non-Kolmogorov statistics. Angle-of-arrival identified the flow to be anisotropic in a region that appeared Kolmogorov using single-component fluid mechanic measurements. Subsequent two-component velocity measurements have verified the optically-detected flow anisotropy. Anisotropy occurs in flow regions where there are large differences between longitudinal and lateral velocity components. Both fluid-mechanic and optical statistics collected along the major flow axis (longitudinal direction) have Kolmogorov statistics, while data collected in directions transverse to the major flow axis (lateral direction) have non-Kolmogorov statistics.

Implications to USAF programs are that non-Kolmogorov turbulence statistics may go undetected using single-component turbulence statistics. An example of single-component turbulence measurements are the fluctuating temperature measurements made during both ABLACE and WWABL experiments. These data sets are not suitable for determining the amount of non-Kolmogorov turbulence in regions of interest. Angle-of-arrival spectra was found to be a more useful means for detecting non-Kolmogorov turbulence statistics. Two-component velocity measurements were also found to be an effective method for detecting non-Kolmogorov statistics and flow anisotropy.

It was also found that non-Kolmogorov statistics occur predominantly in directions of low mean velocity. For atmospheric turbulence, it can be expected that non-Kolmogorov

statistics would be found in two directions, one direction horizontal and normal to the direction of predominant wind, the second direction being the vertical direction.

Based on the results of this investigation, it is anticipated that it would be more difficult to detect optical anisotropy during vertical transmission than during horizontal transmission. Vertical transmission usually involves transmission through multiple layers that exist at varying altitudes, with each layer having a different mean wind direction. This would tend to wash out the observed anisotropy. **In the event that there is an overall westerly flow pattern, vertical transmission would be expected to have Kolmogorov statistics in the East-West and non-Kolmogorov statistics in the North-South.**

Extending this logic to the scenario of horizontal transmission, it is anticipated that horizontal transmission in the wind direction (either with or against the wind) would display the highest degree of non-Kolmogorov statistics. For the scenario of horizontal transmission either into or with the wind, both horizontal and vertical beam jitter components would have non-Kolmogorov statistics. For horizontal transmission in a direction perpendicular to the mean wind direction, the horizontal beam jitter component would be Kolmogorov while the vertical jitter component would be non-Kolmogorov.

2. ACCOMPLISHMENTS / NEW FINDINGS

The research has considered turbulence measurements in a non-isothermal free shear flow, with specific emphasis placed on examining non-Kolmogorov turbulence statistics. A heated axisymmetric jet has been investigated. The report first describes the experimental facility and associated fluid-mechanic and optical measurement equipment used to perform the investigation, followed by an experimental results section presenting the turbulence statistics collected in the heated jet.

2.1. Experimental Apparatus

Experimental measurements were performed on a heated axisymmetric jet using both fluid mechanic and optical measurements. Fluid mechanic measurements of velocity and temperature were made using a pitot-static tube, thermocouple, and thermal anemometer. Optical measurements were made using one-dimensional optical wavefront sensors and lateral-effect detectors for angle-of-arrival (jitter) sensing.

2.1.1. Heated Jet Facility

A heated axisymmetric jet, shown schematically in Fig. 1, forms the free shear flow under investigation. The jet facility is capable of generating jet velocities (U) from 1 m/s to approximately 16 m/s with jet-exit temperatures on the order of 15°C above ambient. The jet consists of a 16:1 contraction ratio nozzle, with a nozzle exit diameter of 12.7 mm. An automated traversing mechanism (not shown in Fig. 1) was installed on the surrounding optical bench, enabling flow surveys to be conducted as far downstream as twenty nozzle diameters from the jet exit plane. Jet conditions for the results presented here are with a jet exit velocity of 10.5 m/s and a centerline temperature of approximately 10°C above the ambient room temperature of 25°C. Jet exit velocity is measured via plenum pressure using an Omega PX277-01D5V temperature compensated pressure transducer, set to read 0-0.25 inches of water with 0-10 V output. Jet exit and room temperature measurements are made using two Omega DP116-KC2 thermocouple readouts.

2.1.2. Fluid-Mechanic Measurements

Mean velocity and temperature measurements are made using the two Omega sensing systems described earlier. Mass-flux measurements are made using Dantec MiniCTA (Model 54T30) modules. Fluctuating temperature measurements are made using a homebuilt Constant Current Anemometer (CCA) system. Approximately 1 mA of current is passed through the constant current wire while making high frequency temperature measurements. Sensing probes are placed on a two-axis traversing mechanism enabling automated data collection. Data acquisition and control of the traversing mechanism was performed using a United Electronic Industries PowerDAQ PD2-MF-16-50/16H 16-bit data acquisition card in conjunction with LabVIEW software.

Two separate sets of fluctuating velocity measurements were made during the investigation. One set of measurements was made with the jet heated (non-isothermal flow) using

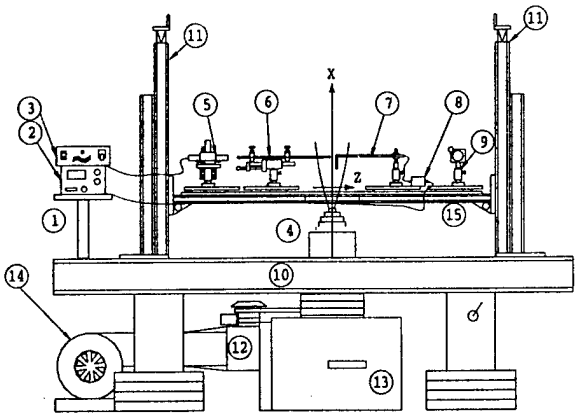

Figure 1. Heated Axisymmetric Jet Facility

a two-wire Dantec Probe (Type 55P62). During these measurements, the upstream probe wire was operated in constant current mode measuring temperature, and the downstream probe wire was operated in constant temperature mode measuring mass flux. The second set of measurements, consisting of two-component velocity, was made with the jet operating without heat (cold or isothermal flow). The cold-flow measurements were made using a Dantec Probe 55P61 (X-wire) and two Dantec MiniCTA systems for each of the constant-temperature wires. Longitudinal and lateral velocity fluctuation measurements were made using the 55P61 probe and associated MiniCTA systems.

I. Non-Isothermal Calibration

Calibration of the CTA and CCA systems for operation under non-isothermal flow conditions are performed by measuring the mean CTA voltage, mean CCA voltage, mean velocity, and mean temperature at a discrete number of operating points spanning the range of conditions to be encountered during the experiments. A King's-law-based[1] empirical fit relating the convective heat transfer coefficient (h) to the flow velocity (U) via a Nusselt number - Reynolds number relationship is used:

$$Nu = a + b\,(Re)^n \tag{1}$$

In this relationship, $Nu = \frac{hd_w}{k_f}$ is the Nusselt number with k_f being the thermal conductivity of air, $Re = \frac{\rho_f U d_w}{\mu_f}$ the Reynolds number, ρ_f the density of air, U the speed of the flow over the wire, and μ_f the viscosity of air. The subscript f refers to properties evaluated at the film temperature of the wire, which is the average of the ambient temperature and the wire temperature ($T_f = \frac{T_\infty + T_w}{2}$). A four-dimensional minimization routine is used in solving for the coefficients a, b, n and T_w which describe the hot-wire's heat transfer characteristics.[2]

II. X-Wire Calibration

The calibration of the 55P61 X-wire sensor was performed using the axisymmetric jet facility, shown schematically in Fig. 2. The velocity data collected using the X-wires was for cold flow, and consequently the calibration was performed under isothermal conditions. The calibration of an X-wire is more complicated than a single hot-wire. The reason for this is that the convective heat transfer from each wire depends on both the magnitude and angle of the flow's velocity vector. In other words, under certain velocity orientations, each sensor is cooled differently depending on the direction of the local flow. In 1977, Willmarth and Bogar[3] presented a multiple angle calibration technique involving a look-up table method. This method requires the X-wire to be pitched at different angles in the free stream, and a velocity sweep performed at each pitch angle. Using the output of each sensor, a look-up table calibration can be developed.[4]

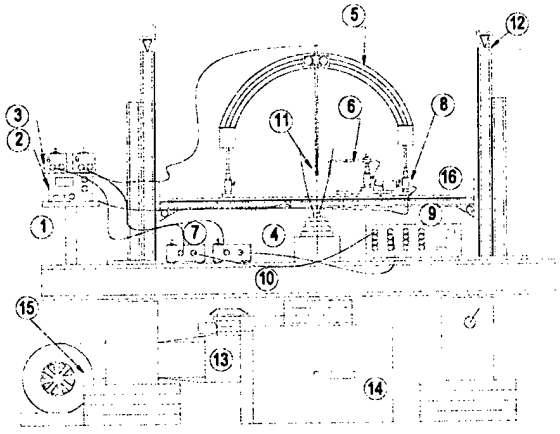

Figure 2. Heated Axisymmetric Jet Facility with X-Wire Apparatus

III. Data Reduction

Data was collected in the heated axisymmetric jet by traversing the hot-wire sensor across the nozzle ($Z-$direction) at varying positions downstream of the jet exit plane ($X-$direction). At each downstream location, the probe was positioned at approximately 30 cross-stream (Y) stations, and data collected for ten seconds at an acquisition rate of 10 kHz. All of the CTA and CCA channels were acquired at each flow station, and written to hard drive in binary for post processing. Prior to sampling, both CTA and CCA channels were low-pass filtered at 1 kHz using a 7th-order, low pass Bessel switched-capacitor filter (Maxim MAX7401).

The first step in the data reduction procedure for non-isothermal flow involved conversion

of the voltages measured by both the CTA and CCA sensors into velocity and temperature time series. Conversion of the CCA voltage into temperature is straightforward involving a linear relationship between voltage and temperature. Conversion of the CTA voltage to velocity is performed by solving for velocity in Eq. 1.[2] Probe-prong conduction begins to effect the wire's frequency response at approximately 0.1 Hz while thermal inertia effects the data for frequencies greater than 100 Hz (assuming a flow speed of 10 m/s). The frequency response limitations[5] of the constant current wire have been compensated for using digital post-processing operations.[6]

The velocity and temperature time series were further processed by computing 2048-point power spectral density (PSD) functions. An ensemble average of 16 PSD's was computed for both velocity and temperature, and a line fit to the spectra in log-log space over wavenumber ($k = 2\pi f/U$ where f is temporal frequency) range 100 to 300.

Hot-wire data collected under cold flow conditions using the X-Wire involved a post-processing operation using a look-up table, as described earlier. Spectra of the X-Wire velocity signals were computed using Matlab. Power spectral density functions of 2048-point velocity data sets were computed. Fifty of these power spectral density functions were collected and ensemble averaged at each flow point.

2.1.3. Optical Measurements

As illustrated in Fig. 1, the optical equipment is mounted onto a 5'×3' vertically-translating optical bench (Item #15) with a 12 inch hole cut in the center allowing the jet to flow up past the sensors mounted on the optical bench. The translating optical bench is positioned with respect to the jet exit plane using two manually-operated vertical translation rails (Items #11 shown in Fig. 1, Velmex Model B9039W1-S9-TSL-BK). This enables the jet flow to be interrogated at streamwise locations ranging from $X/D = 2$ to $X/D = 20$ without requiring realignment of the optics at each streamwise position. Three types of optical measurements have been made in this investigation, consisting of:

- Shack-Hartmann wavefront sensors (SH-WFS);
- Small-diameter single beams transmitting on the jet centerline;
- Small-diameter single beams transmitting off of the jet centerline (Y/D Translation);
- Small-diameter single beams with a control section (Z/D Translation).

I. SH-WFS Measurements

Optical wavefront distortion measurements were made using two one-dimensional Shack-Hartmann wavefront sensors[7,8] (SH-WFS), as shown in Fig. 5. One wavefront sensor was oriented horizontally (perpendicular to the mean-flow axis - Item #3 in Fig. 5) and the other vertically (parallel to the mean-flow axis - Item #5 in Fig. 5). Each sensor consists of a one-dimensional lenslet array (448μm spacing with a lenslet focal length of 3.745 cm) and a Dalsa

CL-C4-2048 line-scan camera (2048 pixels at 14 μm per pixel). A total of 256 frames were collected simultaneously from both cameras with a 5 kHz frame rate via a VME-based data acquisition system, enabling 51.2 ms of wavefront information to be collected per acquisition run.

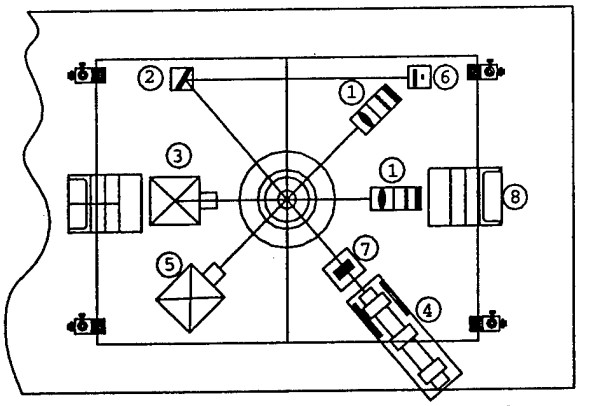

Figure 3. Top View of Translating Optical Bench - SH-WFS and Jitter Measurements

II. Jet-Centerline Beam Jitter Measurements

Angle-of-arrival or beam jitter measurements were made by transmitting a low power (1.5 mW) HeNe laser beam through the center of the jet flow and directing it onto a UDT Sensors Inc. Model SC-10D lateral-effect detector, Item #6 shown in Fig. 5. The lateral-effect detector is a single large-area photodiode that outputs four currents from which the centroidal position of the incident beam is determined. The SC-10D's output currents are conditioned using two UDT Model 301-DIV transimpedance amplifiers (10 kHz frequency response), one for each detector axis.

Spectra of the angle-of-arrival signal were computed using a Hewlett-Packard Dynamic Signal Analyzer (HP 3562A). The spectrum analyzer was controlled remotely via HPIB bus and LabVIEW software running on a PC. Two power spectral density functions were computed, one for the streamwise jitter signal (X-direction) and the other for the cross-stream jitter signal (Y-direction). The majority of the spectra presented in this paper were performed by ensemble averaging one hundred individual spectra collected with a Nyquist frequency of 10 kHz.

III. Off-Centerline Beam Jitter Measurements (Y/D Translation)

The experimental hardware described above was modified to permit the HeNe laser beam and all of the associated optics (two mirrors and the lateral-effect detector) to be traversed to points off of the jet's centerline ($Y/D \neq 0$ in Fig. 4). A custom translating frame system was designed and machined to perform this duty. The translating frame, shown in Fig. 4, permits the laser, directing mirrors, and lateral-effect detector to be moved in unison using a manual

translation stage (Item #9 in Fig. 4, Velmex Model 02515CE-S2.5). This enables the beam to be positioned to transmit through Y/D's off of the jet's centerline without the need to realign the optics at each new measurement location. The translating frame was positioned using the manual translation stage, and the linearity of the motion was ensured using the four guide rails (Item #8) shown in Fig. 4. As before, spectra of the beam jitter signal were computed using a Hewlett-Packard Dynamic Signal Analyzer (HP 3562A) controlled remotely via HPIB bus and LabVIEW software running on a PC.

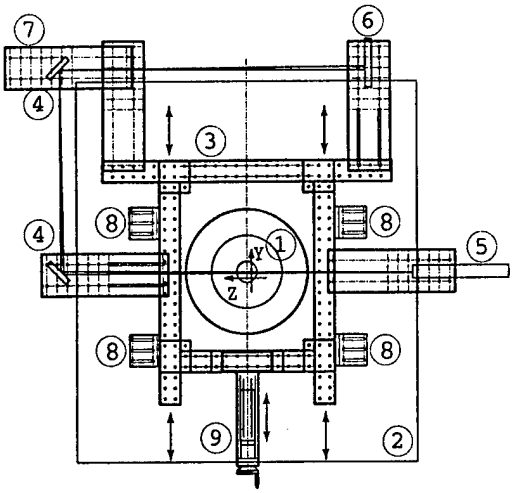

Figure 4. Top View of Translating Optical Bench - Off-Centerline Measurements (Y/D Translation)

IV. Control-Section Beam Jitter Measurements (Z/D Translation)

Two *beam tubes* constructed from 8.13 mm (0.32") OD and 5.08 mm (0.2") ID acrylic tubing were used to shroud part of the beam as it transmitted through the jet flow in the Z-direction, as illustrated in Fig. 5. The space between the two beam tubes, called the *Control Section*, was fixed at 5 mm (0.4 jet diameters = $0.4D$). The angle-of-arrival signal collected across the control section and the fluid mechanic measurements described earlier are physically collocated. Consequently, the angle-of-arrival signal made in the *Control Section* is more closely matched to the single-point fluid mechanic measurements. In order to move the control section in the Z-direction across the jet, a special translating frame system was designed, machined and positioned on the vertically-translating optical bench. This translating frame, shown in Fig. 5, permits the laser, directing optics, and lateral-effect detector to be moved in unison with a manual translation stage (Velmex Model 02515CE-S2.5). This enables the beam control section to be positioned to Z/D locations off of the jet's centerline without the need to realign the optics at each new measurement location. The translating frame was positioned using the manual translation stage, and described earlier, the linearity of the motion were ensured using four guide rails.

Optical angle-of-arrival (jitter) measurements were made by transmitting a small-diameter ($\approx$ 1 mm) HeNe laser through the first beam tube, the *Control Section*, and the second beam tube in a direction perpendicular to the jet's mean flow direction. The off-axis beam position measured using the lateral-effect detector in this manner characterized the optical aberration across the control-section. This is illustrated in Fig. 5, where a top view of the horizontally-translating platform is provided. Again, spectra of the beam jitter signal were computed using a Hewlett-Packard Dynamic Signal Analyzer (HP 3562A) controlled remotely via HPIB bus and LabVIEW software running on a PC.

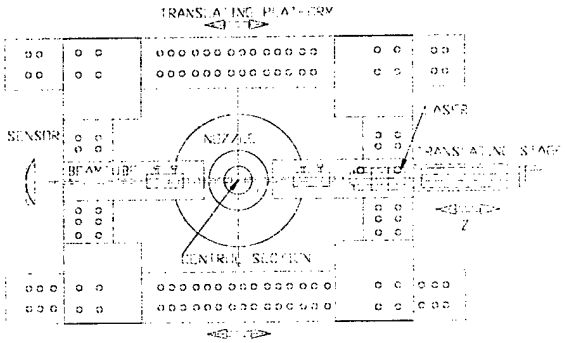

Figure 5. Top View of Optical Bench - Control-Section Measurements (Z/D Translation)

2.2. Experimental Results

This section presents experimental results that have been collected in the heated jet. The first two subsections discuss how it was determined that data was being collected within the inertial subrange of turbulence. This is followed by sections that present turbulence results collected using both fluid mechanic and optical measurements.

2.2.1. The Inertial Subrange - Outer Scale

Investigation of turbulence statistics first requires verification that the spectral range under investigation coincides with the inertial subrange of turbulence. In order to do this, long duration cross-stream beam jitter spectra for transmission through the jet's centerline were collected at $X/D = 10$ with *flow on* ($U = 10.5$ m/s) and with *flow off* ($U = 0$ m/s). Long duration spectra give an indication of where the outer scale lies, and where the inertial subrange begins. One set of these spectra, collected with a Nyquist frequency of 100 Hz, is shown plotted in Fig. 6. Both the *flow on* and *flow off* spectra are identical for frequencies below 5 Hz. Spectral energy in the angle-of-arrival signal for frequencies below 5 Hz is most likely attributed to room currents sensed by the beam while transmitting outside of the jet. Consequently, it can be concluded that the jet contributes little to spectral energy below 5 Hz with the jet operating at $U = 10.5$ m/s.

The *flow on* and *flow off* spectra are seen to depart at frequencies above 5 Hz, with the *flow off* spectra dropping rapidly towards an electronic noise floor by 100 Hz. The difference between the *flow on* and *flow off* spectra is attributed to the aberrating effects of the heated jet. The *flow on* spectra is noted to begin to approach a power-law relationship (f^{-n} with $n = 1$) at frequencies above 50 Hz. A power law relationship is expected in the inertial subrange of turbulence. Consequently, it can be concluded that the inertial subrange is approached for frequencies above approximately 50 Hz.

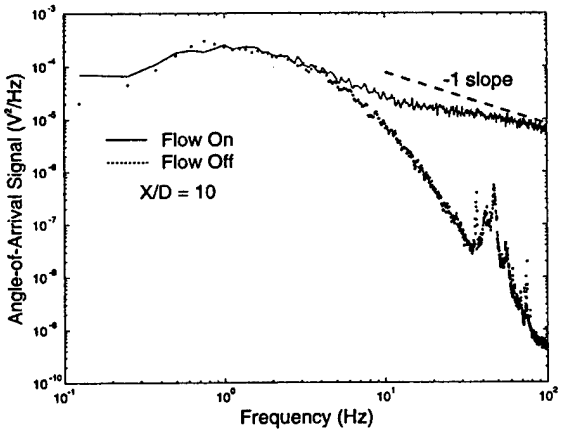

Figure 6. Onset of Inertial Subrange in Horizontal Angle-of-Arrival Spectra

2.2.2. The Inertial Subrange - Inner Scale

The inner scale of turbulence can be estimated from the eddy dissipation rate (ϵ) using the well known relationship[10]:

$$\eta = \left(\frac{\nu^3}{\epsilon}\right)^{1/4} \tag{2}$$

where η is the inner scale and ν is the kinematic viscosity. The eddy dissipation rate is related to the velocity structure parameter C_v^2, which can be determined using the "spectral method" as described by Wyngaard et al.[11] Eddy dissipation rate is then determined from C_v^2 using the relationship $C_v^2 = 2\epsilon^2/3$, as outlined by Kaimal.[12] The velocity structure parameter C_v^2 is equal to the magnitude of the velocity power spectral density function at wavenumber one. A velocity power spectral density function collected at $X/D = 10$ is shown plotted in Fig. 7. Velocity spectra using two different hot wires are shown on this figure, one collected using a Dantec Model #9055 P31 (55P31) with a 1 mm active sensing length and the second collected using a Dantec Model #9055 P62 (55P62) with a 3 mm active sensing length. The signal from each hot wire was filtered using a low-pass filter set at 5 kHz. Considering that the flow velocity at $X/D = 10$ was around 3.4 m/s, the effects of the low-pass filter would not be evident until wavenumbers greater than 9000.

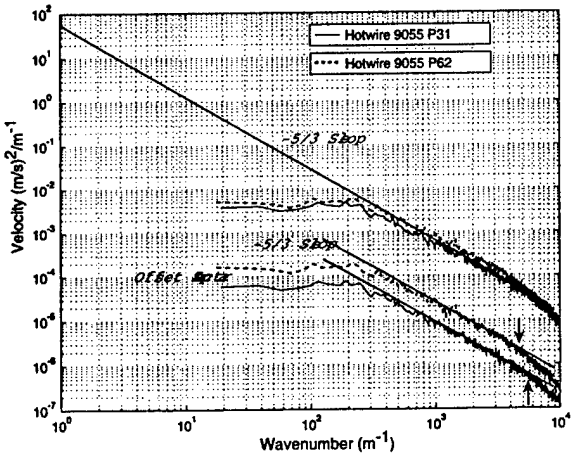

Figure 7. Determining Inner Scale using Single Hot Wire

For illustrative purposes the two spectra have been offset and separated in the bottom part of Fig. 7, where it is noted that the 55P62 deviates from the -5/3 power law relationship at a lower wavenumber than the 55P31. From the figure, spectral roll-off due to inner scale appears to begin at a wavenumber between 5000 and 6000, suggesting that the inner scale is less than 0.2 mm. A more accurate inner scale estimate can be made by first determining the magnitude of C_v^2, and then using the equation outlined by Kaimal.[12] Using this method,

the velocity structure parameter C_v^2 is found to be approximately 50 and the inner scale 0.07 mm.

2.2.3. Fluid Mechanic Statistics

This subsection presents data collected in the heated axisymmetric jet using pitot-static tube, thermocouple, constant temperature, and constant current anemometers. Data is presented for flow surveys from two to eighteen nozzle diameters downstream of the jet exit plane. At each downstream location, data was collected by traversing the anemometers in the cross-stream (Y/D) direction.

I. Mean Flow Statistics - The Gradient Fields

Mean flow statistics are collected using both a pitot-static tube for the mean velocity and a thermocouple for the mean temperature. The axisymmetric jet flow is characterized by the mean flow in the cross-stream (horizontal) direction having larger gradients than the flow in the streamwise (vertical) direction. Mean flow gradients result in turbulence generation. By comparing the streamwise velocity gradient field to the cross-stream gradient field in Fig. 8, it is noted that the cross-stream gradient field is much larger.

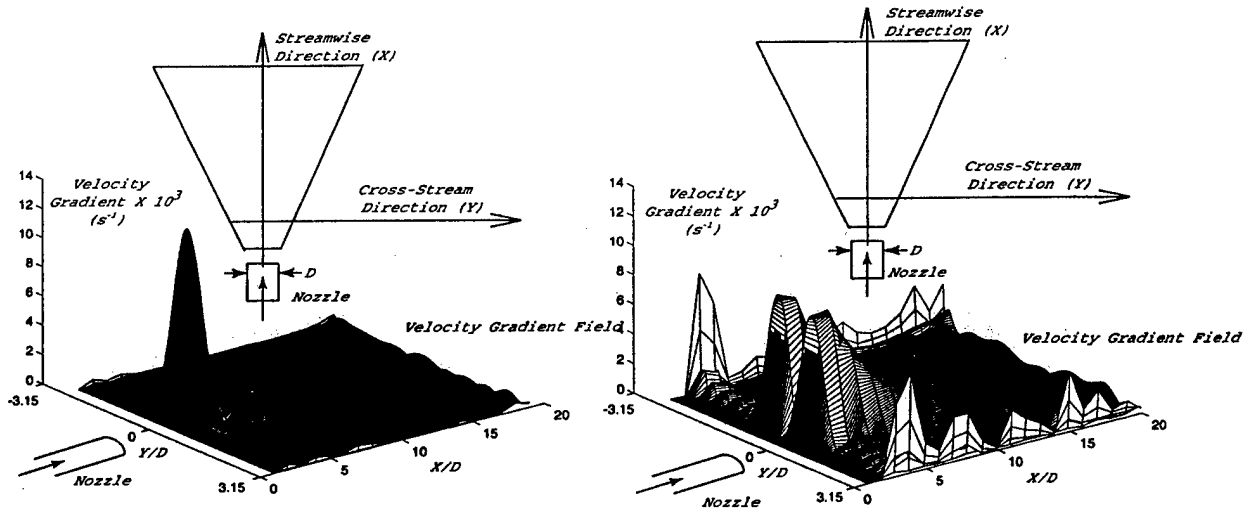

Streamwise Direction Cross-Stream Direction

Figure 8. Velocity Gradient Field: $Y/D = 0 \rightarrow 20$

A more detailed comparison is given in Fig. 9 at $X/D = 10$ where the velocity gradient profile in the cross-stream direction is noted as being up to four times larger than the velocity gradient in the streamwise direction. Given that the mean shear is what drives turbulence production, anisotropy in the mean flow gradients is in part responsible for anisotropy in turbulence statistics.

The gradient field of the mean temperature is shown plotted in Fig. 10. The streamwise temperature gradient field is shown plotted on the left of Fig. 10, where it can be seen

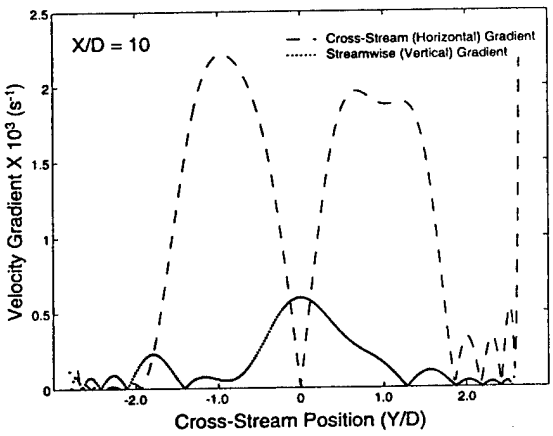

Figure 9. Velocity Gradient Profile at $X/D = 10$

that the largest gradients, although somewhat random, exist near the jet's centerline. The cross-stream gradient field, plotted on the right in Fig. 10, shows higher and more organized gradients that correspond to the jet's central regions.

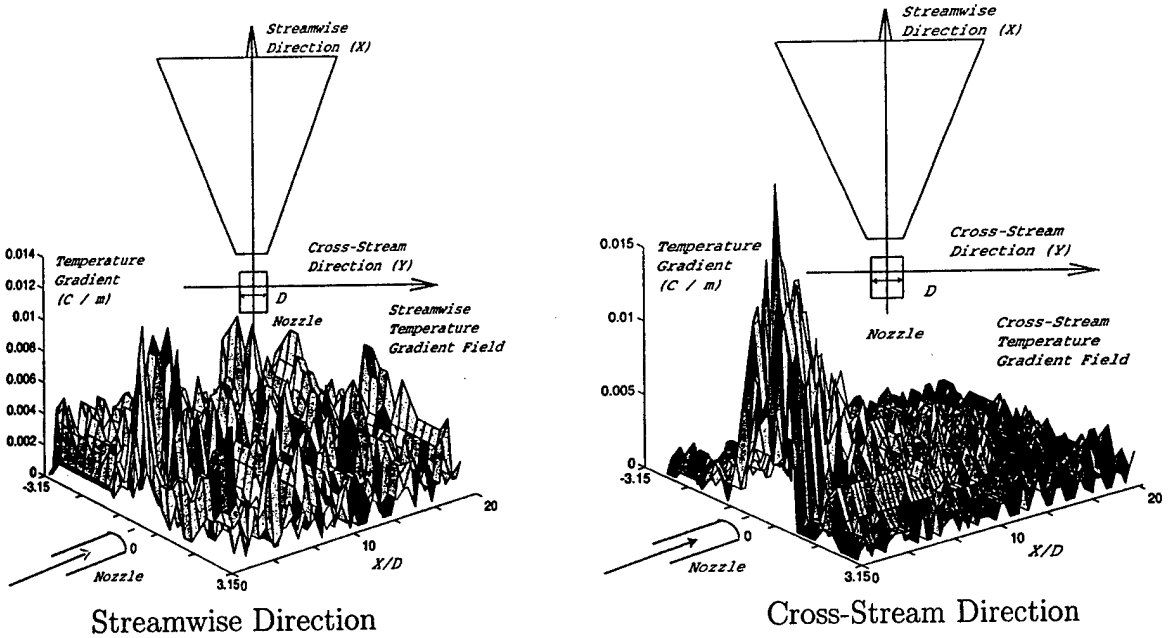

Streamwise Direction Cross-Stream Direction

Figure 10. Temperature Gradient Field: $Y/D = 0 \rightarrow 20$

II. Spectral Statistics

Spectra of the velocity and temperature fluctuations, collected at five nozzle diameters downstream of the jet exit plane ($X/D = 5.0$), is shown plotted in Fig. 11. It should be noted that these velocity spectra are collected in non-isothermal flow using a single hot wire anemometer, and consequently they represent the total velocity fluctuation rather than the

longitudinal and lateral components as collected using an X-Wire. Spectra between the jet's centerline to one-half diameter off of the centerline ($Y/D = 0.5$) are shown in these figures, from which it can be seen that the velocity spectra change more with cross-stream (Y/D) position and depart further from the characteristic -5/3 spectral slopes than do temperature spectra. In order to further assist in understanding spectral change with cross-flow position, contour maps of the power spectral density functions and spectral slopes were plotted as a function of cross-stream position. The following subsections will use both contour maps and spectral slopes to examine the jet's characteristics.

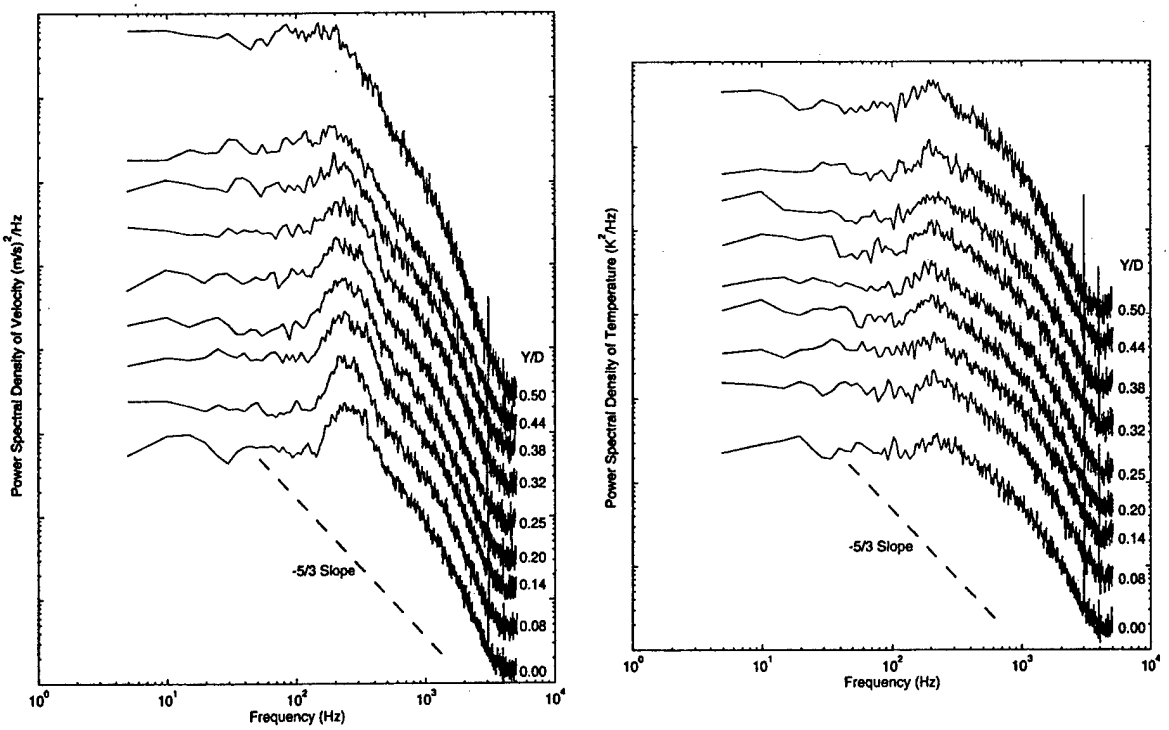

Velocity Temperature

Figure 11. Cross-Stream Spectral Development: $X/D = 5.0$, $Y/D = 0.00 \rightarrow 0.50$

III. Spectra and Spectral Slopes: $X/D = 1.0 \rightarrow 6.0$

Contour plots of velocity and temperature spectra are shown in Figs. 12 and 13 for data collected from $X/D = 1.0$ to $X/D = 6.0$. Figure 12 presents spectra collected between $X/D = 1.0$ and 3.0. As can be seen, the spectral energy for both velocity and temperature fluctuations vary significantly with cross-flow position, showing regions of significant turbulence energy at around 1000 Hz at $X/D = 1.0$. The regions of strong energy are confined to the jet's shear layer, and are centered around $Y/D = \pm 0.5$. Regions near the jet's centerline denote the potential core and are void of both mechanical and temperature turbulence. As the jet's shear layer undergoes the rollup process, vortex structures begin to pair with one another, halving the primary disturbance frequency from 1000 Hz at $X/D = 1.0$ to approximately 500 Hz at $X/D = 2.0$. By $X/D = 3.0$ energy in the velocity spectra is noted to

extend across the jet's collapsing potential core region, spanning from $Y/D = 0.5 \rightarrow -0.5$. Temperature spectra collected at the same streamwise location do not exhibit high spectral energy near the jet's centerline. The reason for this is that velocity fluctuations are integrative and result from all of the vorticity present in the flow, whereas temperature fluctuations are local and result due to mixing between hot and cold fluid at a specific point in the flow.

Figure 13 presents spectra collected between $X/D = 4.0$ and 6.0. This region is characterized by the jet's large scale vortical structures transitioning from organized discrete structures confined to narrow spectral regions ($X/D = 4.0$ on the jet's centerline) to a flow where the spectral energy is distributed more broadly over a wider range of frequencies ($X/D = 6.0$, also on the jet's centerline). This process results due to nonlinearities in the Navier-Stokes equation which serve to transfer spectral energy from discrete frequency bands to a broad range of frequencies. The spectral contour plots at $X/D = 6.0$ indicate a trend where spectral energy is seen to decrease with increasing frequency. Spectral energy is found to drop off in an exponential manner, resulting in linear slopes when the spectra are plotted in log-log space indicating the presence of an inertial subrange.

Spectral slopes for both velocity and temperature fluctuations collected between $X/D =$ 1.0 and 6.0 are shown plotted as a function of cross-stream location in Fig. 14. The spectral slopes are noted to be widely varying with cross-stream position, with values ranging from -6 to 1. This variability is caused by spectral spikes, and the amount of variability is noted to decrease with downstream position as flow nonlinearity causes spectral energy to be transferred from the discrete spikes to a broader range of frequencies, resulting in smoother spectra. Spectral slope values are found to converge close to the -5/3 value expected for Kolmogorov turbulence. A slight difference is noted between spectral slopes for velocity and temperature. It is believed that this difference is due to the complications of the signal conditioning procedure required for operating hot-wire anemometers in non-isothermal flows.

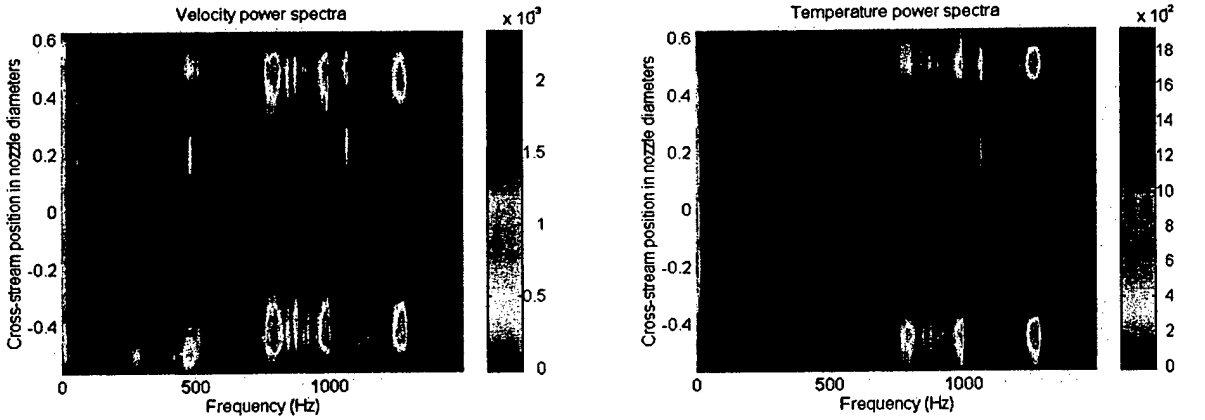

$X/D = 1.0$

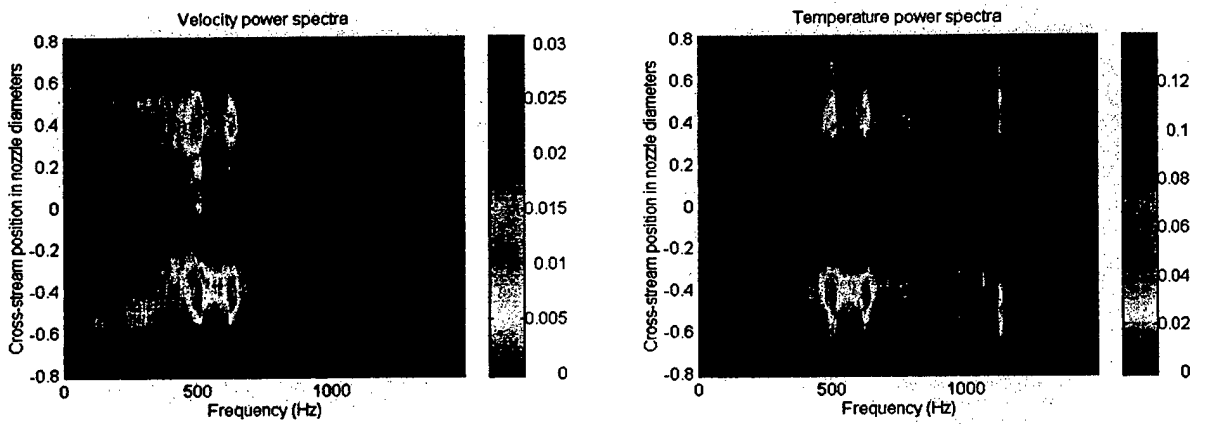

$X/D = 2.0$

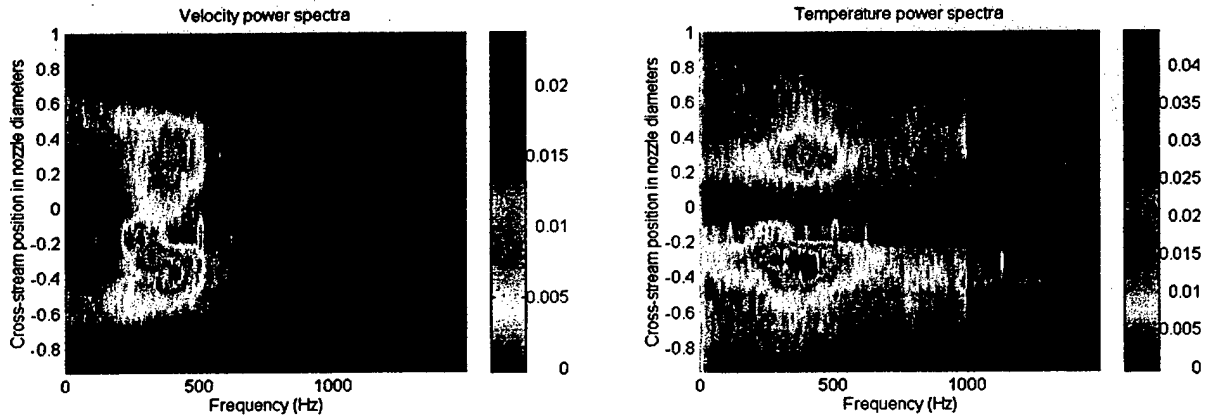

$X/D = 3.0$

Figure 12. Cross-Stream Spectral Contour Maps - $X/D = 1.0 \rightarrow 3.0$

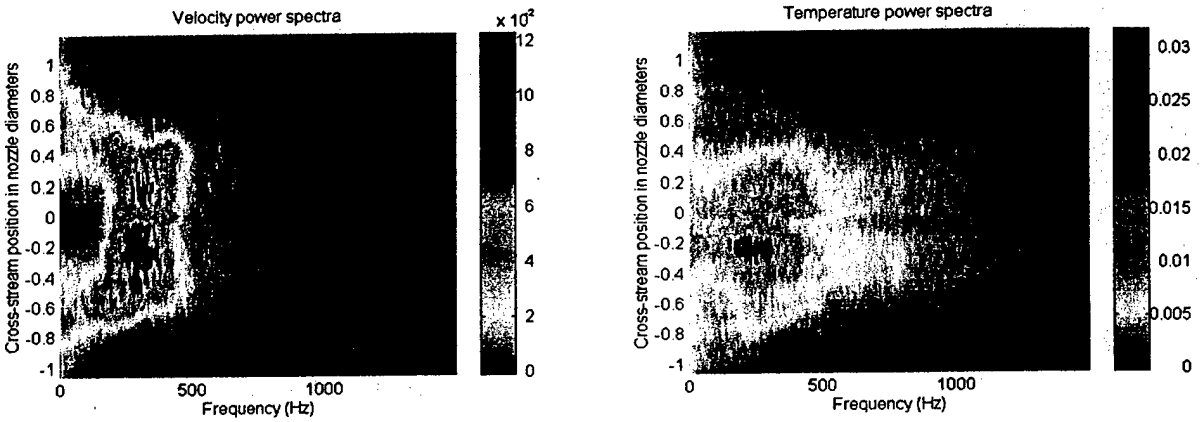

$X/D = 4.0$

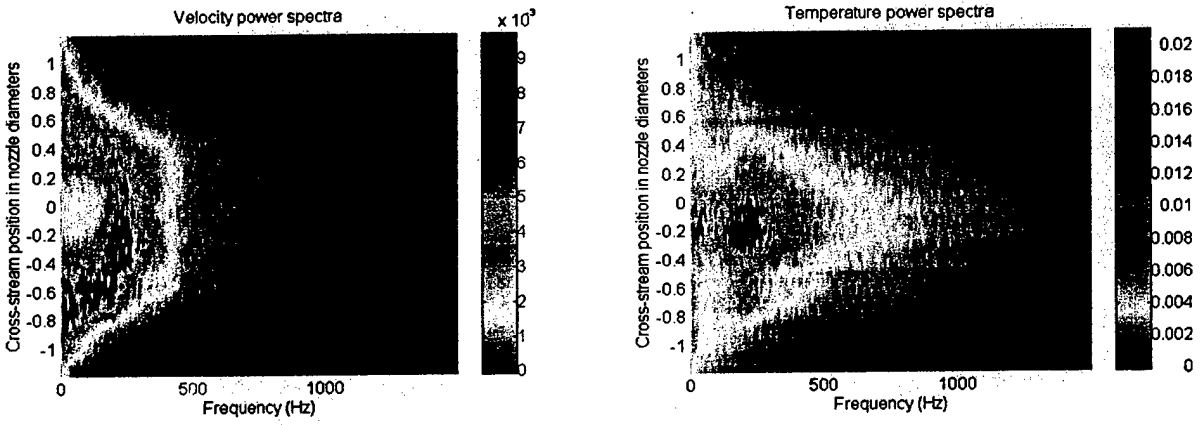

$X/D = 5.0$

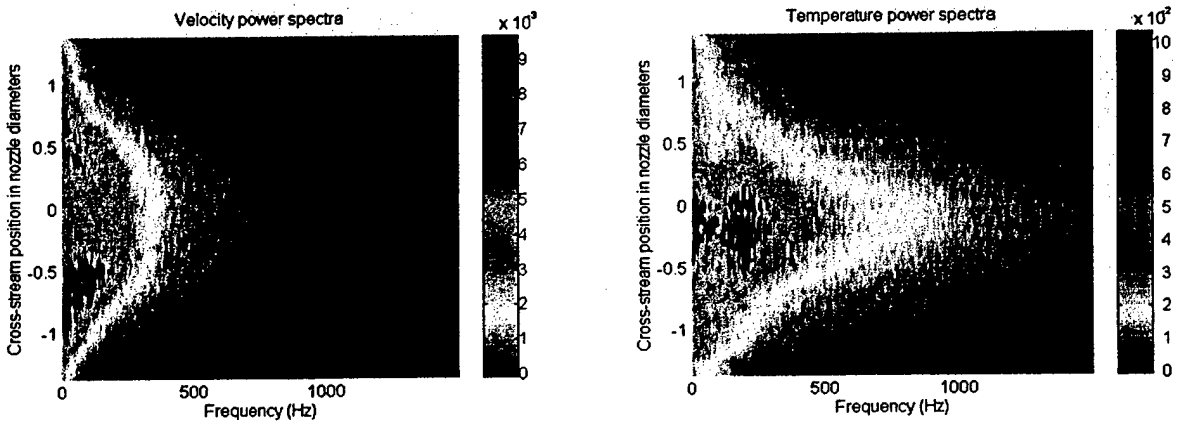

$X/D = 6.0$

Figure 13. Cross-Stream Spectral Contour Maps - $X/D = 4.0 \rightarrow 6.0$

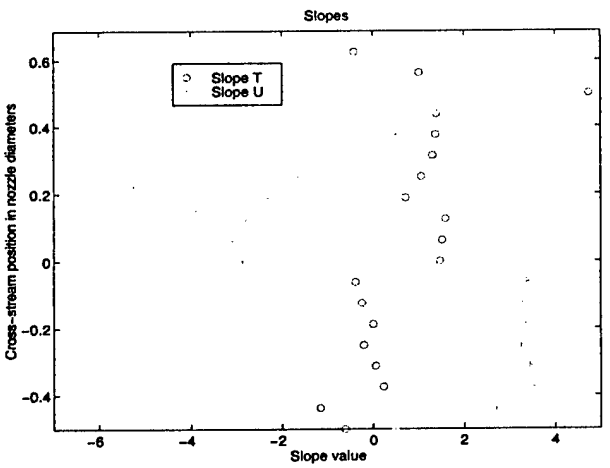

$X/D = 1.0$

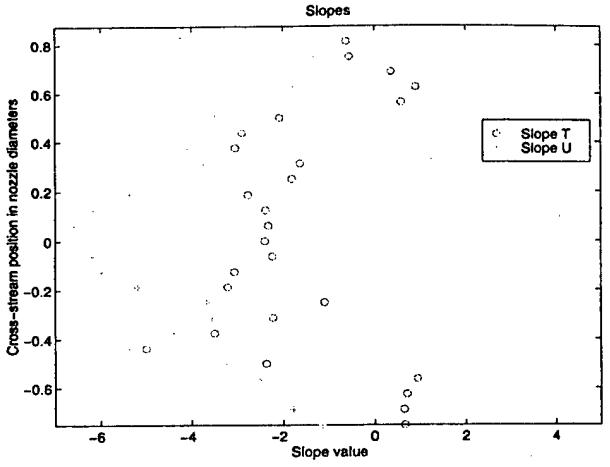

$X/D = 2.0$

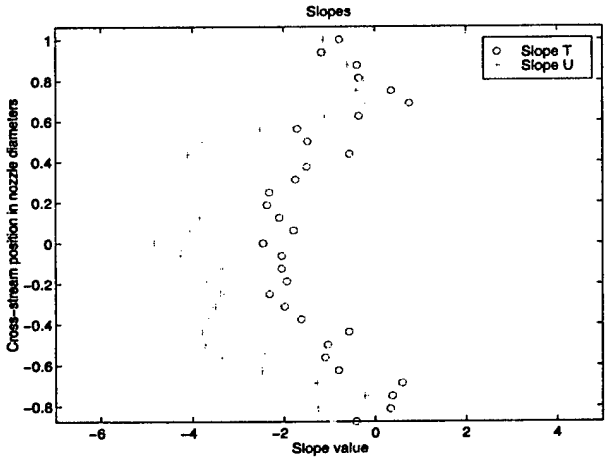

$X/D = 3.0$

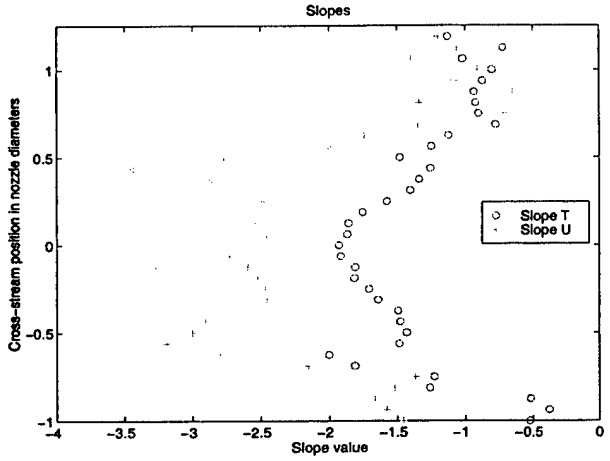

$X/D = 4.0$

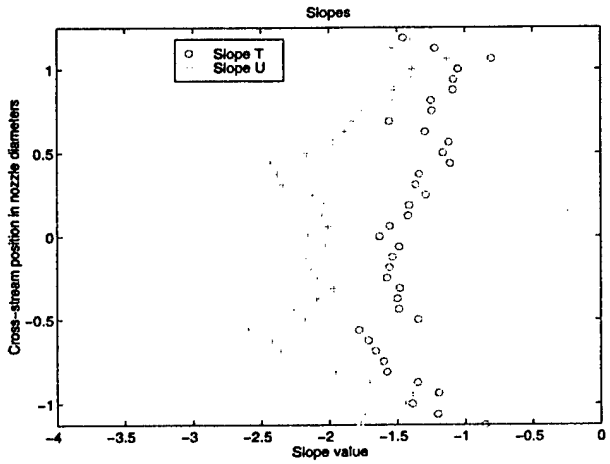

$X/D = 5.0$

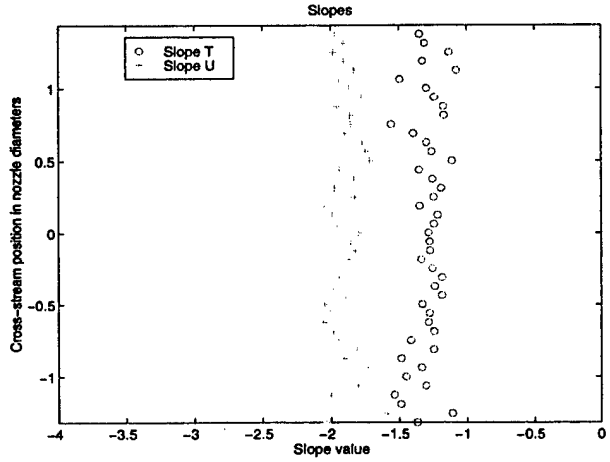

$X/D = 6.0$

Figure 14. Cross-Stream Spectral Slopes - $X/D = 1.0 \rightarrow 6.0$

IV. Spectra and Spectral Slopes: $X/D = 8.0 \rightarrow 18.0$

Contour plots of velocity and temperature spectra are shown in Figs. 15 and 16 for data collected between $X/D = 8.0$ and $X/D = 18.0$. These spectra show no evidence of spikes, and all of the spectral energy is noted to decrease smoothly with increasing frequency. It should be mentioned that the contour plots between $X/D = 8.0$ and $X/D = 18.0$ cover a wider range of the flow with increasing distance from the nozzle exit plane, ranging from 3 diameters width at $X/D = 8.0$ to 5.5 diameters width at $X/D = 18.0$. This widening process is associated with a decrease in the magnitude of the spectra, as evidenced by the absence of spectral energy above 100 Hz.

Spectral slopes collected between $X/D = 8.0$ and $X/D = 18.0$, shown plotted in Fig. 17, are seen to become relatively invariant with increasing downstream position. This indicates that the flow has transitioned to fully developed turbulence, with values for both velocity and temperature found to be near -5/3. These slope values are close to what would be expected for Kolmogorov turbulence, and based on these spectra alone it would be easy to conclude that the turbulence has Kolmogorov statistics.

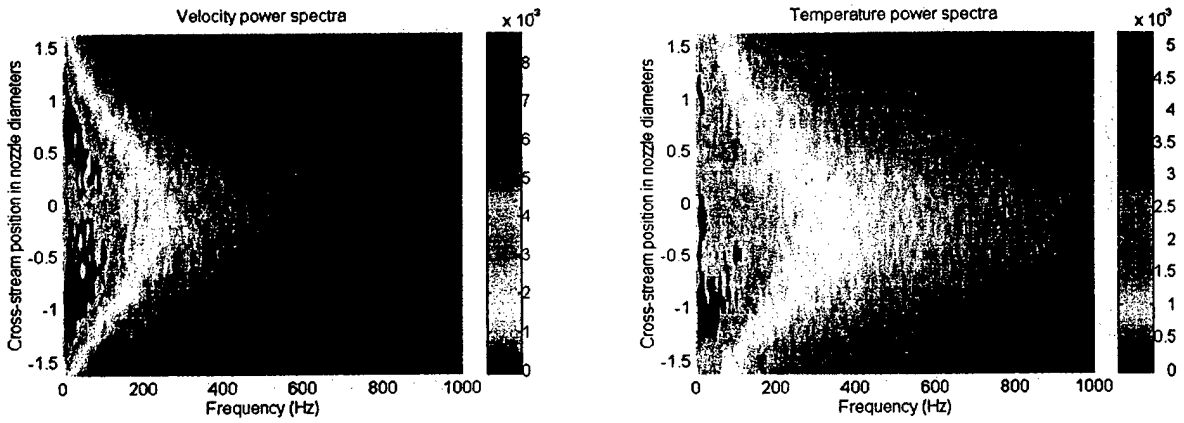

$X/D = 8.0$

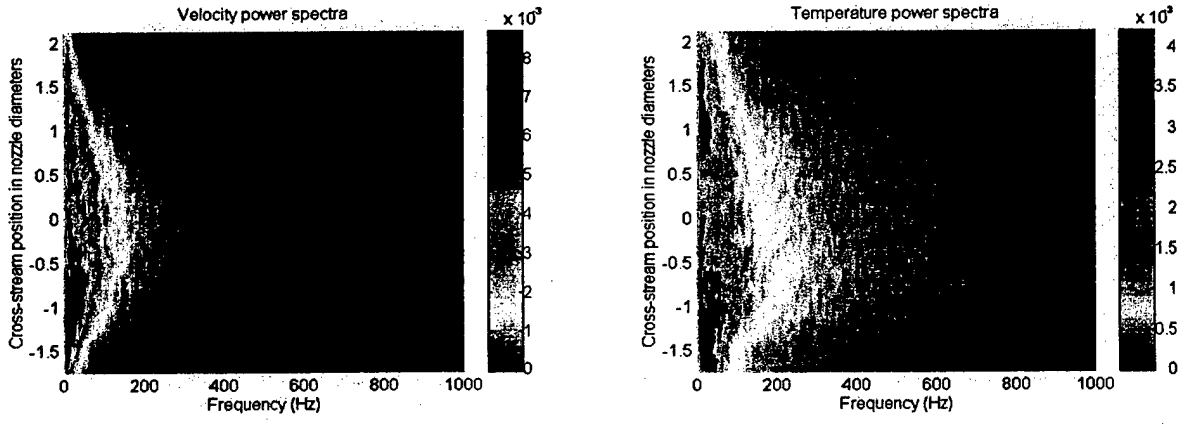

$X/D = 10.0$

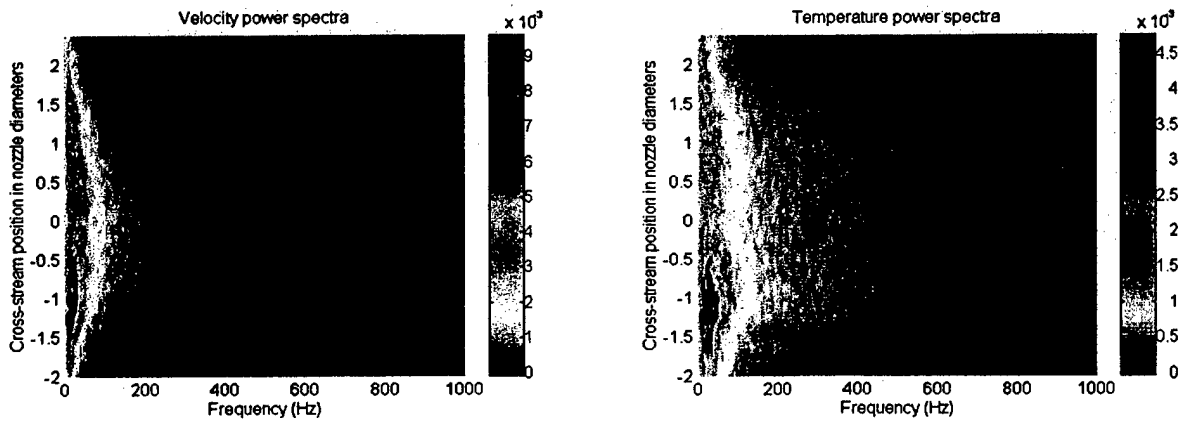

$X/D = 12.0$

Figure 15. Cross-Stream Spectral Contour Maps - $X/D = 8.0 \rightarrow 12.0$

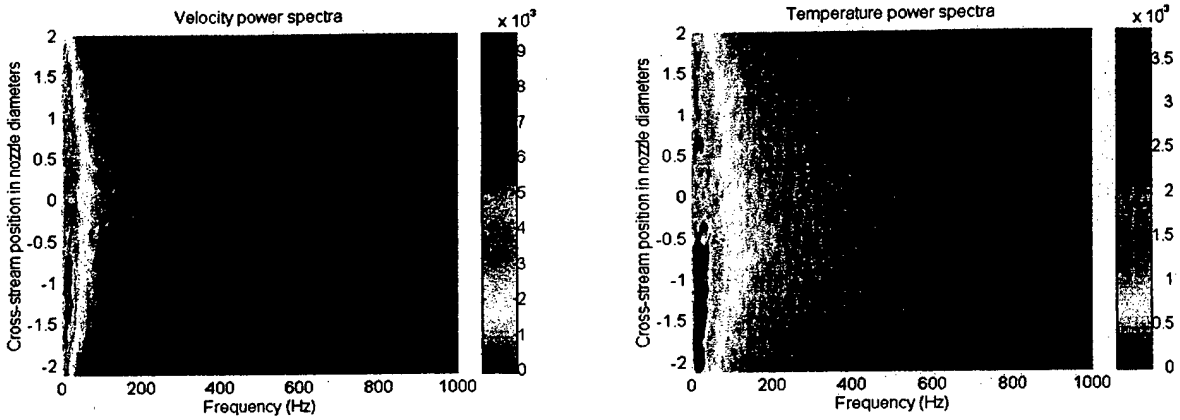

$X/D = 14.0$

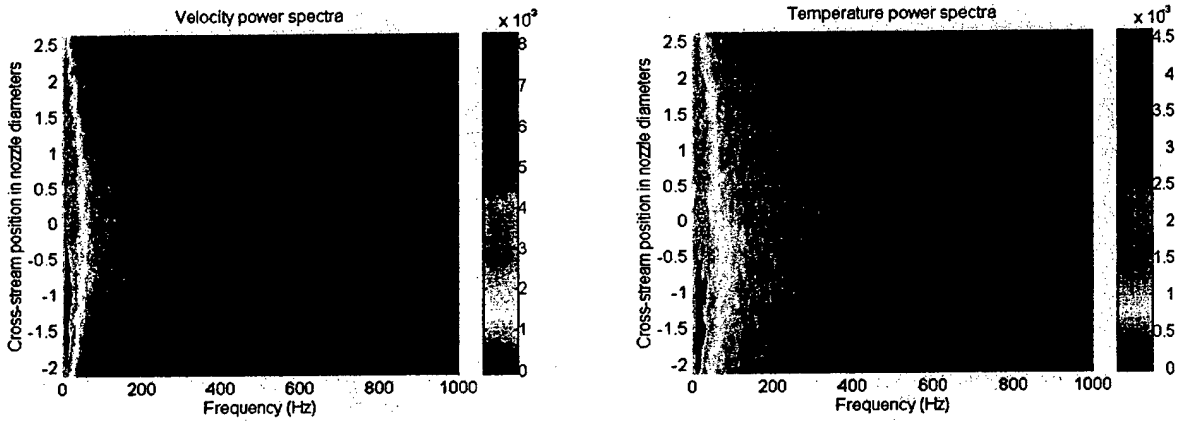

$X/D = 16.0$

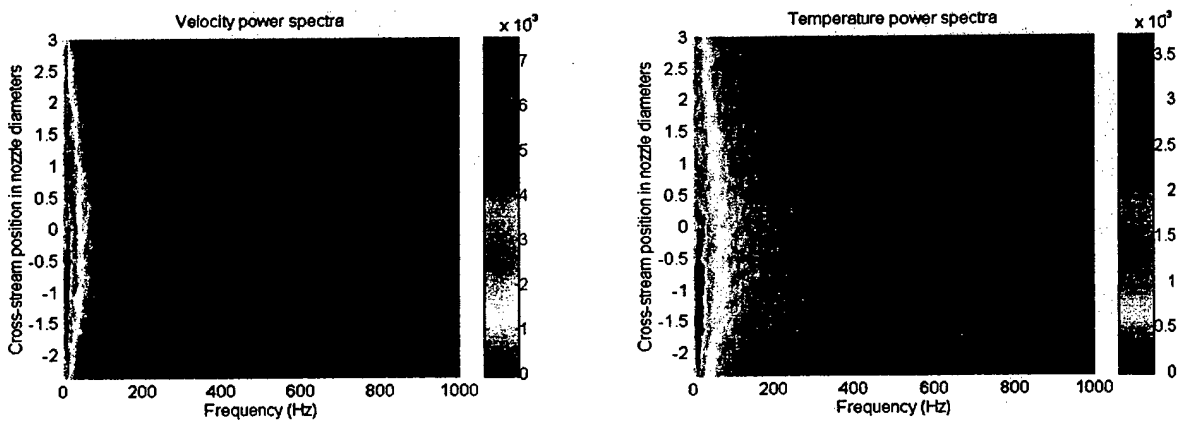

$X/D = 18.0$

Figure 16. Cross-Stream Spectral Contour Maps - $X/D = 14.0 \rightarrow 18.0$

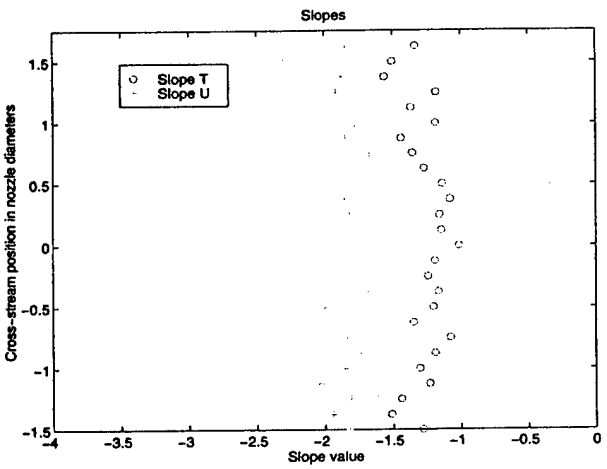

$X/D = 8.0$

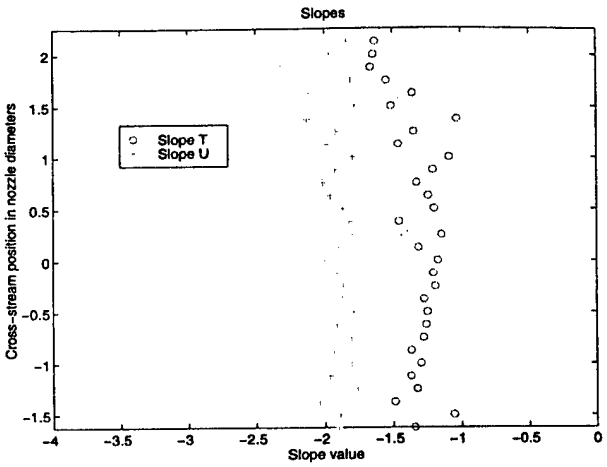

$X/D = 10.0$

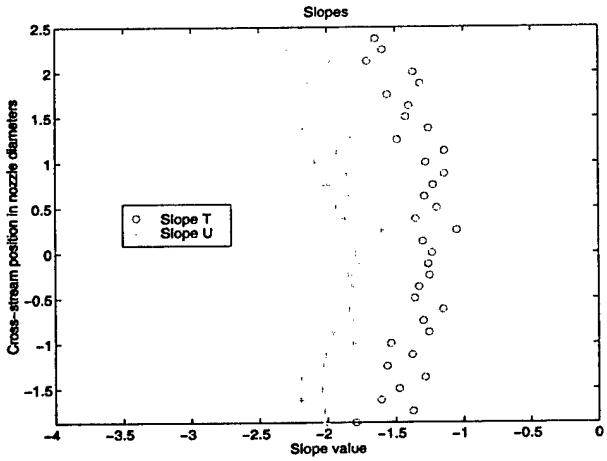

$X/D = 12.0$

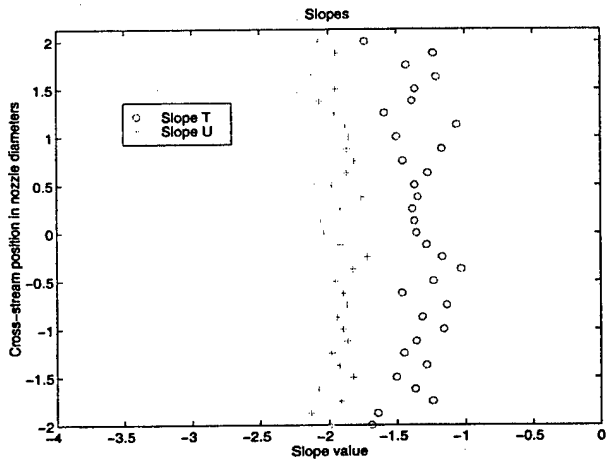

$X/D = 14.0$

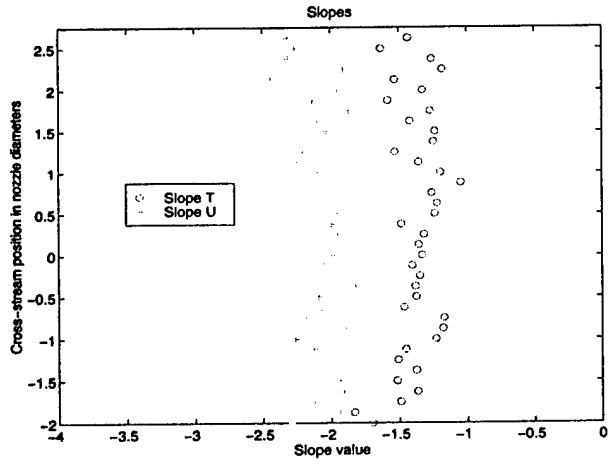

$X/D = 16.0$

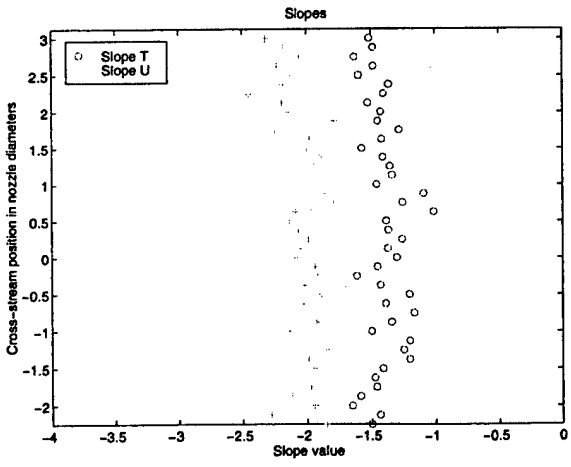

$X/D = 18.0$

Figure 17. Cross-Stream Spectral Slopes - $X/D = 8.0 \rightarrow 18.0$

V. Mean and Variance of Spectral Slopes: $X/D = 1.0 \rightarrow 18.0$

A condensed representation for how the power spectral density functions change with downstream position can be obtained by plotting the mean and variance of spectral slopes at each downstream location. The mean and variance of the spectral slopes collected at each downstream position are shown plotted in Fig. 18, where it is observed that the variance of the spectral slopes decreases to near zero when the mean of the spectral slopes nears a value of -5/3. This is seen to occur at around $X/D = 5.0$. Referring back to the spectral contour plots in Fig. 13, this occurs at a location where large spectral spikes are no longer evident in the power spectral density functions.

By examining both the mean and variance of the spectral slopes in Fig. 18, it can be concluded that, based on single-point fluid-mechanic measurements, the heated axisymmetric jet can be characterized as having Kolmogorov statistics for positions downstream of $X/D =$ 6.0. Spectral slopes other than -5/3 are associated with formation regions of turbulence[9] where velocity shear produces large-scale coherent structures through the Kelvin-Helmholtz instability mechanism. For the axisymmetric jet, the formation region is confined to the first six nozzle diameters downstream of the jet exit plane.

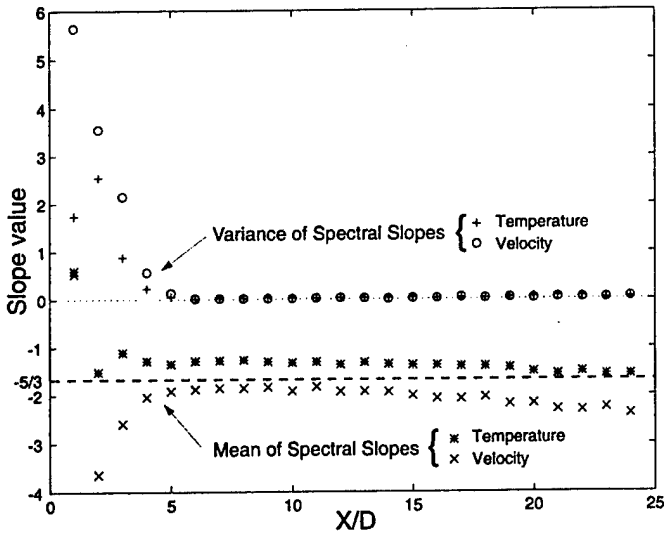

Figure 18. Spectral-Slope Development with Streamwise Position

The evolution of the jet flow can also be examined by plotting the power spectra of the constant temperature anemometer signal (mass flux) collected along the jet's centerline. This has been done in Fig. 19, from which it can be seen that the centerline mass flux signal attains Kolmogorov statistics (-5/3 slope) by $X/D = 7.0$. It is interesting to examine the spectra collected at $X/D = 6.0$ which shows no direct evidence of the large scale structure seen in spectra upstream of this point yet the spectral slope is steeper than the Kolmogorov -5/3 value. Spectral development between $X/D = 11$ and 20 reveals a consistent slope of -5/3 in the power-law region.

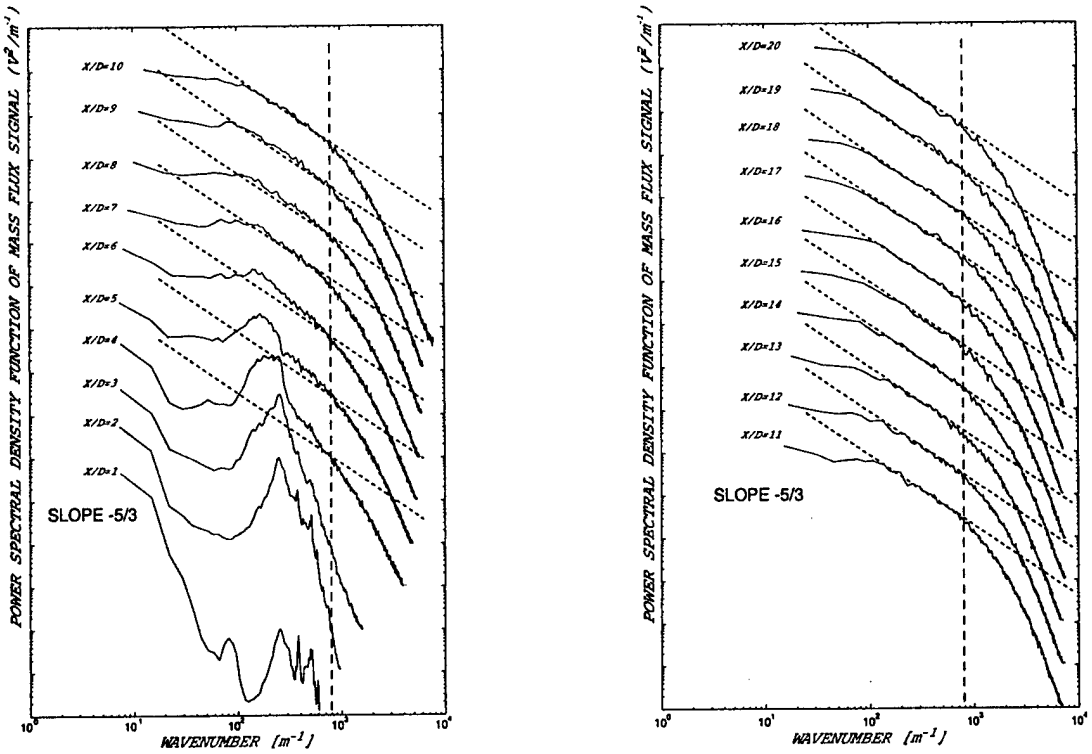

$X/D = 1 \rightarrow 10$ $\qquad$ $X/D = 11 \rightarrow 20$

Figure 19. Hot-Wire (Mass Flux) Spectral Development $X/D = 1 \rightarrow 20$

VI. X-Wire Spectra

Figure 20 shows the X-Wire spectra collected at $X/D = 10$ in both the horizontal (lateral) and vertical (longitudinal) directions, with the low-pass filter beginning to effect the spectra between 2 and 3 kHz. While collecting this data, the X-Wire was traversed in the Z direction through the centerline of the jet (cf. Fig. 5). The spectra collected using the X-Wire illustrate anisotropy in turbulence statistics, with the lateral velocity signal having spectral slopes of -4/3 and the longitudinal velocity signal having slopes of -5/3. Spectra collected near the center of the jet ($Z/D = 0$) reveal the strongest spectral energy. If we take into consideration the range of eddies of scale $r \ll l_0$ where l_0 is the inner scale of turbulence, the slope of the power spectra in this range can be expressed to the power -3. At these scales the turbulence turns into laminar flow with no preferred direction. The weaker spectra collected from the edge of the jet indicate a narrowing in the frequency range over which a noticeable inertial subrange exists.

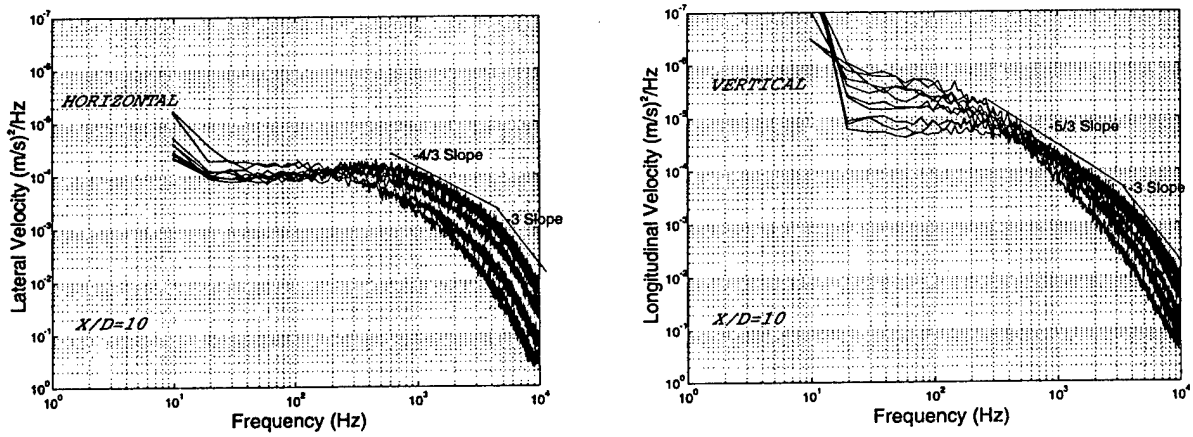

Lateral Longitudinal

Figure 20. X-wire Spectra collected at $X/D = 10$ with varying Z/D

Figure 21 presents both lateral and longitudinal X-Wire spectra collected at the jet's centerline ($Z/D = 0$), at increasing streamwise locations from $X/D = 10 \rightarrow 20$. The power-law relationship for the lateral velocity spectra exhibits $f^{-4/3}$ behavior while the longitudinal velocity exhibits $f^{-5/3}$. Although the strength of the turbulence is noted to decrease with downstream position, the extent of the inertial subrange does not change as significantly as it does with varying Z/D in Fig. 20.

Figure 22 shows the longitudinal (vertical) and lateral (horizontal) X-Wire spectra collected with the low-pass filter's cutoff frequency set at 5 kHz. While collecting this data, the X-Wire was extended through the centerline of the jet in the same manner as performed at $X/D = 10$ in Fig. 20. Velocity fluctuation spectra show power-law behavior (a straight line in log-log space) in the inertial subrange, extending between the integral scale, where energy is injected, and the inner scale, where kinetic energy is transferred into thermal energy. The

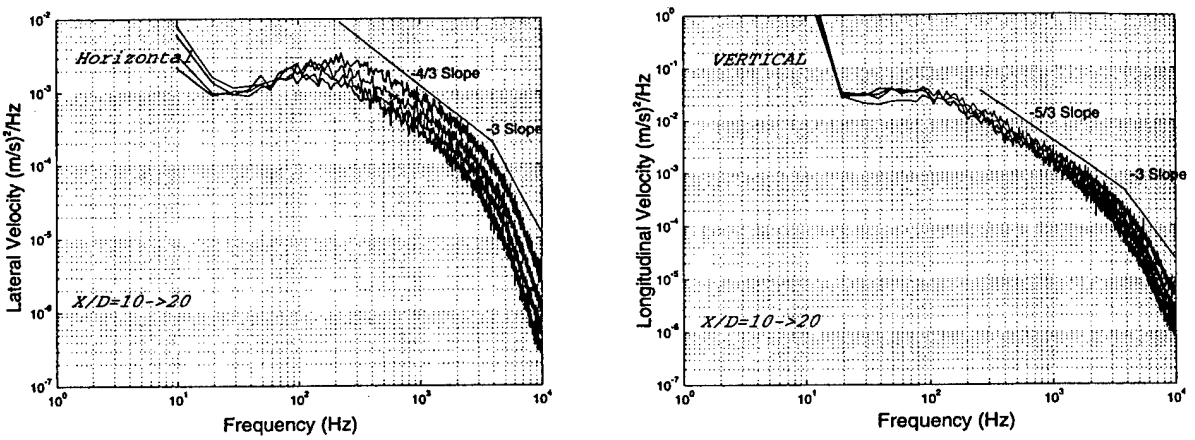

Lateral Longitudinal

Figure 21. X-wire Spectra collected at $Z/D = 0$ and ranging from $X/D = 10 \rightarrow 20$

power-law relationship for the longitudinal X-Wire spectra exhibits $f^{-5/3}$ behavior throughout the entire inertial subrange. The lateral X-Wire spectra, however, shows $f^{-4/3}$ behavior near the integral scale that eventually approximates $f^{-5/3}$ behavior at higher frequencies. This results due to increased isotropy at small scale sizes. Flow anisotropy is also confirmed by examining the velocity variance in Fig. 23, with the longitudinal velocity variance being up to three times larger than the lateral velocity variance.

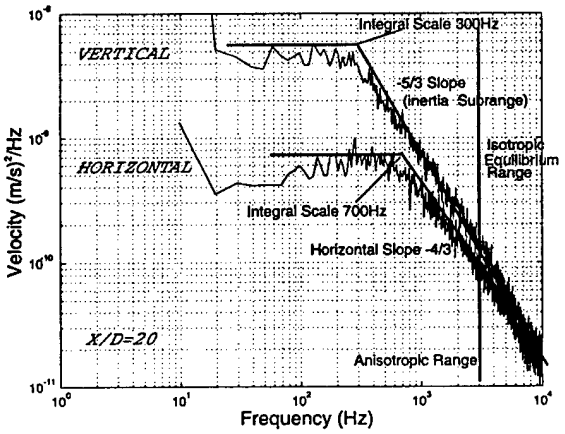

Figure 22. Vertical and Horizontal X-wire Spectra at $X/D = 20$

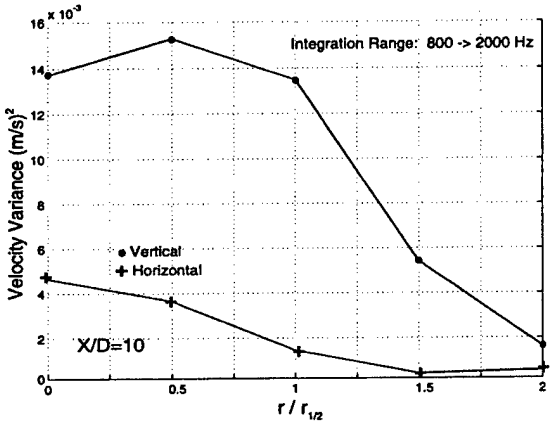

Figure 23. Velocity Variance

2.2.4. Optical Statistics

Two types of optical measurements were made during the investigation. These consisted of:

- Shack-Hartmann wavefront sensors (SH-WFS);
- Small-diameter single beam transmitting through the jet.

The optical wavefront measurements made using the Shack-Hartmann wavefront sensors will be discussed first.

I. Optical Wavefront Measurements using SH-WFS

As mentioned in Section 2.1.3, optical wavefront measurements were performed by collecting 256 frames (51.2 ms of data) of line-scan data over a 28.672 mm one-dimensional aperture. Each wavefront sensor has 64 subapertures across the 28.672 mm aperture, with each subaperture providing the local spatial wavefront slope. Representative time series of the wavefront slope or jitter are shown in Fig. 24 as color contour plots. The color of the contour corresponds to the magnitude of the jitter signal, white being a positive deflection angle and black a negative. The bottom time series was collected with the SH-WFS aligned vertically and centered about $X/D = 2.0$. Distinct patterns can be observed moving up and to the right throughout the image. These lines correspond to the periodic large-scale vortical structures that are present near the nozzle exit. These same periodic structures result in the spikes that were noted earlier in the power spectral density functions (cf. Fig. 12). The time series shown at the top of Fig. 24 was collected with the SH-WFS centered about $X/D = 19.0$. At $X/D = 19.0$ the characteristic structures are moving slower, as evidenced by the angle of the streaks. An increasing angle with respect to the vertical indicates that the structures take a longer period of time to travel the same distance. It is also interesting to note that streaks with different angles are present in the image, an indication that structures are convecting at different velocities.

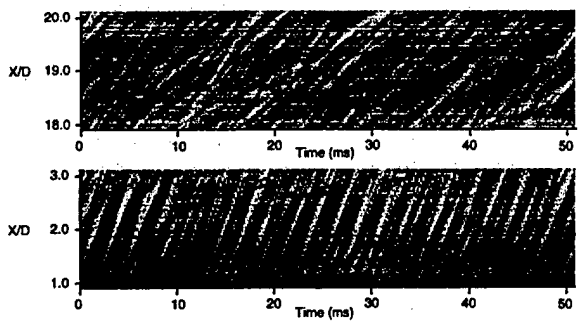

Figure 24. Jitter Time Series Collected using Vertical SH-WFS

The optical wavefronts, in the form of optical path difference, are obtained by spatially integrating the local wavefront slopes from Fig. 24. Optical wavefronts collected from the jet

flow are shown in Fig. 25. These wavefronts have been obtained using both a horizontally-aligned and a vertically-aligned SH-WFS. The data presented in Fig. 25 was collected at four downstream locations: X/D = 4.0; 8.0; 12.0; and, 20.0. As with the jitter time series discussed earlier, periodic structures can be seen in the data collected at X/D = 4.0. Turbulence statistics are computed using the optical wavefront measurements. These statistics consist of both structure functions and spectra.

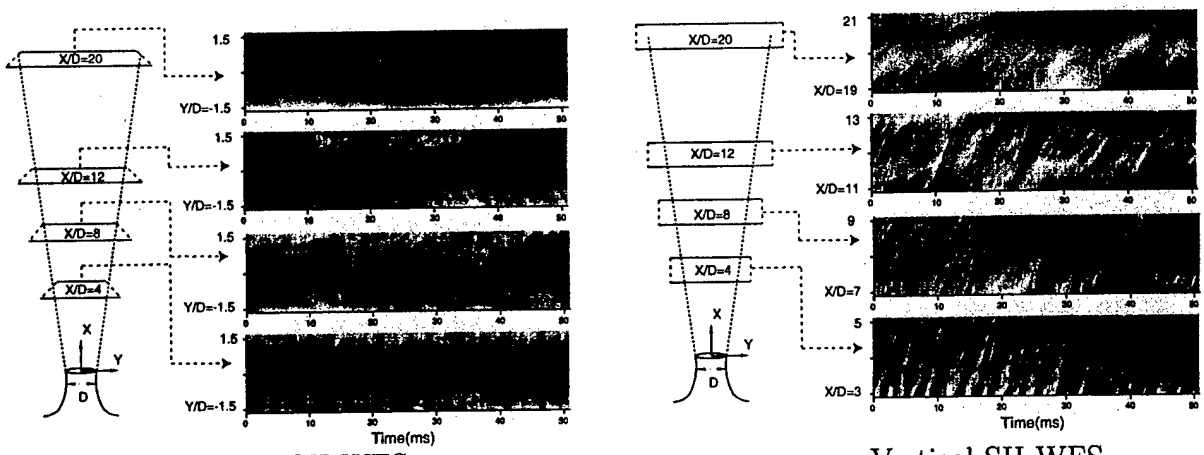

Horizontal SH-WFS Vertical SH-WFS

Figure 25. Optical Path Difference collected at Four Downstream Locations

(i) Structure Functions using SH-WFS Data

Several different methods can be found in the literature for examining Shack-Hartmann wavefront sensor data to determine the statistical character of the optical turbulence that the light has transmitted through. Dayton et al.[13] used the phase structure function

$$D_\phi(r) =< |\phi(r') - \phi(r'+r)|^2 > \tag{3}$$

where ϕ is the optical phase, r spatial separation, and angled brackets denote time averaging. Dayton et al.[13] also used the phase-difference (jitter) structure function

$$D_{\Delta\phi}(r) =< |\Delta\phi(r') - \Delta\phi(r'+r)|^2 > \tag{4}$$

to examine Shack-Hartmann wavefront sensor data for non-Kolmogorov statistics. The phase structure function has a 5/3 slope for Kolmogorov turbulence, while the phase difference structure function has a non-linear relationship with spatial separation r when plotted on a log-log scale.

A generalized phase spectrum (Φ_ϕ) has been used in the literature to describe non-Kolmogorov turbulence statistics,

$$\Phi_\phi(k) = \frac{A_\beta k^{-\beta}}{\rho_o^{\beta-2}} \tag{5}$$

where k is wavenumber, β is the power-law exponent of the phase spectrum and ρ_o is a generalized coherence length. Nicholls et al.[14] used the ratio of transverse over longitudinal differential angle-of-arrival variances to determine the slope of the phase spectrum ($-\beta$), and noted values other than $-11/3$ indicating non-Kolmogorov optical turbulence. Rao et al.,[15–17] claiming better performance by removing the effects of measurement noise, used the differential angle-of-arrival fluctuation coefficient and the slope structure-correlation coefficient to determine β. Rao et al.[16] presented data illustrating both Kolmogorov and non-Kolmogorov phase statistics.

With only one-dimensional wavefront sensing hardware available during this investigation, it is not possible to compute the functions presented by Nicholls et al.[14] and Rao et al.[15–17] as these methods require two-dimensional Shack-Hartmann wavefront sensor data. Consequently, it was decided to use the methods outlined by Dayton et al.[13] and to compute the phase structure and phase-difference (jitter) structure functions.

Figure 26 presents the phase structure function, computed using Eq. 3 and the data from the vertically-aligned SH-WFS. The phase structure function was computed at a location near the nozzle ($X/D = 2.0$) where the flow is known to have fluid-mechanic-based spectra that exhibit non-power-law behavior and at a location further downstream ($X/D = 20$) where the fluid-mechanic-based statistics exhibit power-law behavior. The two phase structure functions have been duplicated and offset towards the bottom of the figure in order to compare their slopes. The two curves are noted as having different slopes, with the data from $X/D = 20$ having the lesser slope. In the figure the two offset structure functions have been bounded on either side by the expected 5/3 slope for Kolmogorov turbulence. It is interesting to note that the phase structure function at $X/D = 2$ is closer to the 5/3 Kolmogorov slope than the data collected at $X/D = 20$. This result is surprising due to the fact that, based on the fluid-mechanic measurements presented earlier, one would expect the $X/D = 20$ phase structure function to be closer to Kolmogorov power-law behavior than the $X/D = 2$ data.

Figure 27 presents the phase-difference (jitter) structure function computed using Eq. 4 and data from the vertically-aligned SH-WFS. As mentioned earlier, the jitter structure function behaves non-linearly when plotted on a log-log scale. Again, jitter structure functions collected at both $X/D = 2$ and $X/D = 20$ were duplicated and offset towards the bottom of the figure in order to perform a more detailed comparison between curves. The results of this comparison show the jitter structure function to be nearly identical up to a separation of approximately 2 mm for data both from $X/D = 2$ and $X/D = 20$. For separations larger than 2 mm, the two jitter structure functions are seen to diverge from one another.

A comparison of the phase structure functions collected under fully-developed turbulence conditions at $X/D = 20$ for both the horizontal and vertical SH-WFS's are shown in Fig. 28.

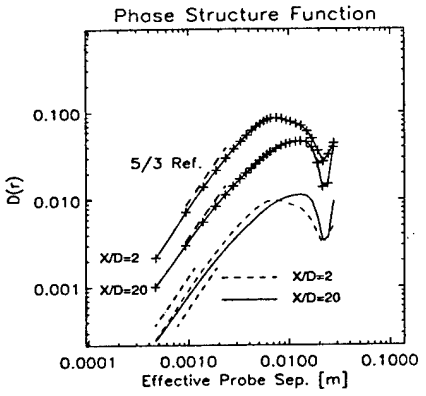

Figure 26. Phase Structure Function at $X/D = 2$ & 20: Vertical SH-HWS

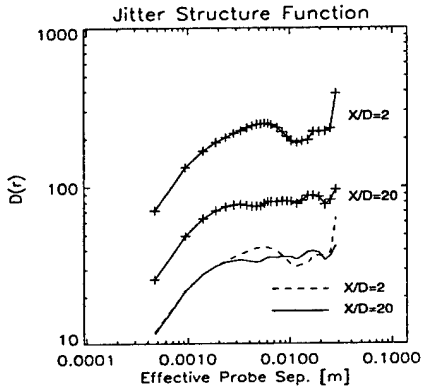

Figure 27. Jitter Structure Function at $X/D = 2$ & 20: Vertical SH-HWS

The structure function from the vertical SH-WFS is offset vertically so that the two structure functions intersect at a separation of 1 mm. The vertical structure function indicates a linear relationship over a larger range of probe separation than that for the horizontal structure function. The two structure functions also indicate different slopes. It is, however, difficult to determine whether this slope difference is attributed to an actual difference in slope or just due to a leveling off of the structure function itself.

(ii) Jitter Spectra using SH-WFS Data

In order to investigate the relationship between horizontal and vertical SH-WFS statistics further, ten sets of horizontal and vertical SH-WFS data were collected at $X/D = 8$ and 20. Each subaperture of the SH-WFS measured angle-of-arrival data at an acquisition rate of 5 kHz, resulting in ten sets of 256-point angle-of-arrival time records. Spectra were computed for each of these 256-point data sets, and then ensemble averaged. An example of the resulting spectra, computed using horizontal jitter data collected at two cross-stream locations at $X/D = 8$, is shown in Fig. 29. The spectra computed using the SH-WFS appear jagged as only 10 ensemble averages have been performed. The number of ensemble averages was kept low at ten due to the large storage space requirements for raw linescan data.

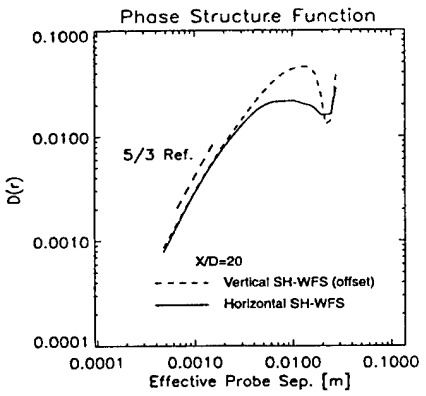

Figure 28. Phase Structure Function at $X/D = 20$: Horizontal and Vertical SH-HWS

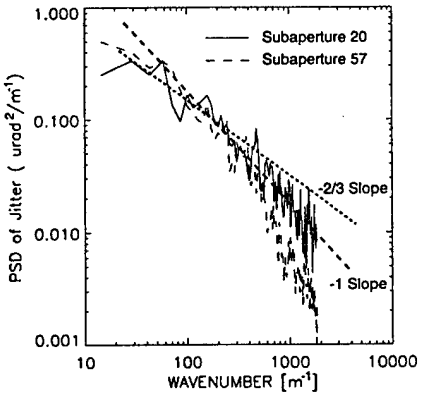

Figure 29. Horizontal SH-HWS Jitter Spectra at $X/D = 8$

The two spectra shown in Fig. 29 have been plotted in terms of wavenumber ($k = 2\pi f/U$). The jet's centerline velocity was used to compute wavenumber in these spectra. This operation is erroneous as the jet velocity at both Subaperture #20 and Subaperture #57 is different from the jet's centerline velocity. Although the error does not alter spectral slopes, it does have an effect on the wavenumber at which the spectra departs from power-law behavior. This can be seen in Fig. 29 where the spectra for Subaperture #57 departs from power-law behavior earlier, at a lower wavenumber, than the spectra for Subaperture #20. Spectra depart from power-law behavior due to aperture averaging, a spatial averaging process that occurs across each detector's subaperture. Each subaperture of the SH-WFS is 448μm wide, and consequently the effects of aperture averaging should become evident by a wavenumber of approximately 2200.

Plotting spectra with wavenumber computed using a velocity higher than the actual velocity translates the entire spectra up and to the left, however, it does not rotate the spectra. Consequently, spectral slope estimates should not be affected by this error. It is, however, possible for the spectral-slope fit range to extend into a region where the spectra departs from power-law behavior, resulting in erroneous spectral-slope estimates.

Power-law relationships with slopes of -1 and -2/3 have been shown in Fig. 29. The rationale for plotting a line with a slope of -2/3 is that jitter spectra are expected to follow this type of power-law relationship under Kolmogorov turbulence conditions. The expected spectral slope under Kolmogorov turbulence conditions can be determined by relating the wavefront phase spectra to the jitter spectra. Rao et al.[17] state that the wavefront phase temporal power spectrum should follow $f^{-(\beta-1)}$ in high frequency where f is the temporal frequency. They show spectra of the wavefront phase with a slope of $-8/3$ for Kolmogorov turbulence. Malley et al.[18] present a relationship between power spectra of optical path difference (OPD) and power spectra of angle of arrival as

$$k^2 \Phi_{OPD} = \Phi_{\epsilon_x} \tag{6}$$

where k is the wavenumber ($= 2\pi f/U$) and ϵ_x is angle of arrival (jitter). Optical path difference can be converted into wavefront phase through the optical wavelength (λ) and Eq. 6 can be rewritten as

$$k^2 \left(\frac{\lambda}{2\pi}\right)^2 \Phi_\phi = \Phi_{\epsilon_x} \tag{7}$$

Based on Eq. 7, converting wavefront phase spectra to a jitter spectra requires multiplying the wavefront phase spectra by k^2. This means that jitter spectra for Kolmogorov turbulence should have a slope of $-8/3+2 = -2/3$. This is the slope of one of the lines drawn in Fig. 29.

Spectra computed from each subaperture of the horizontal SH-WFS collected at $X/D = 8$ and $X/D = 20$ was fit with a "best fit" line over wavenumber range $k = 200 \rightarrow 1000$ and the resulting spectral slopes plotted in Fig. 30. It can be seen that the spectral slopes of the horizontal jitter data do change with cross-stream position and that almost all of the values are lower than the $-2/3$ slope expected for Kolmogorov turbulence. It is also noted that the change in slope across the SH-WFS's aperture is more significant at $X/D = 8$ than at 20. The change in spectral slope with cross-stream position is attributed to the use of the centerline velocity at both $X/D = 8$ and 20 to compute wavenumber. As discussed earlier, this process translates the spectra up and to the left, causing the fit range to extend into the region where aperture averaging causes the spectra to diverge from a power-law relationship.

Velocity change with cross-stream position is more significant at $X/D = 8$ than at $X/D = 20$, and consequently the effects of aperture averaging on the linear fit region result in the larger change in spectral slopes across the viewing aperture. The change in spectral slope is parabolic across the SH-WFS's aperture and is functionally similar to the mean velocity profile across the jet.

Similar spectra were computed using the vertical SH-WFS data. In this case, the sensor was aligned at the center of the jet and the velocity change along the SH-WFS aperture was minimal. Consequently, the wavenumber computed at each subaperture was correct and the errors associated with fitting a line in the aperture averaging region were minimized.

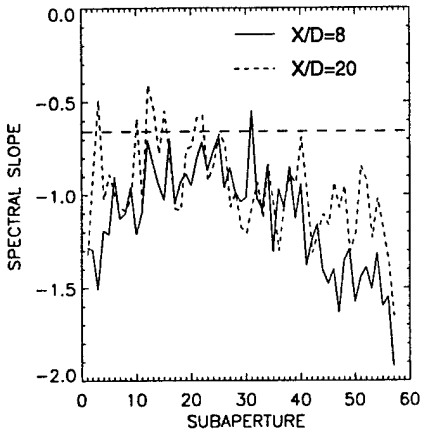

Figure 30. Horizontal SH-HWS Jitter Spectral Slopes

Figure 31 shows two sample spectra collected using the vertical SH-WFS at $X/D = 8$, from which it can be seen that both spectra have similar slopes that follow the -2/3 line up until wavenumber $k \approx 2000$.

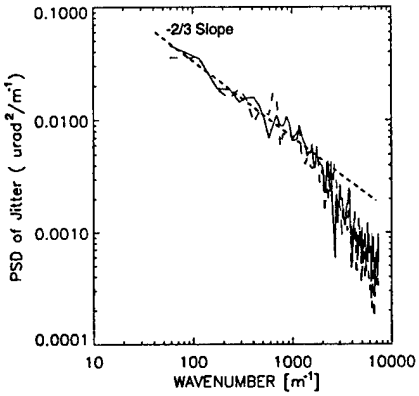

Figure 31. Vertical SH-HWS Jitter Spectra

As for the horizontal SH-WFS data, spectral slopes were fit to the vertical jitter data and plotted as a function of subaperture location. Fig. 32 shows that the spectral slopes for the vertical jitter data remain close to the Kolmogorov $-2/3$ value both at $X/D = 8$ and $X/D = 20$.

Comparing horizontal spectral slopes in Fig. 30 with the vertical spectral slopes in Fig. 32, it is found that the horizontal spectral slopes are largest near the jet's centerline (Subaperture #20) and then decrease towards the jet's edge, with slope values staying below the Kolmogorov -2/3 for most of the SH-WFS's viewing aperture. The vertical spectral slopes plotted in Fig. 32 show spectral slopes that are centered about the Kolmogorov -2/3 value. All of the computed spectral slopes show a significant amount of scatter. The scatter results from the limited number of ensemble averages that were performed while computing these

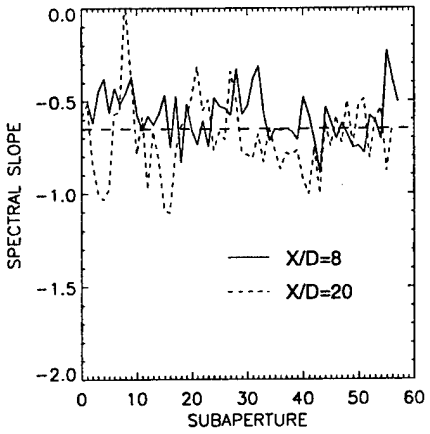

Figure 32. Vertical SH-HWS Jitter Spectral Slopes

spectra. This problem is addressed in the next section where single small-aperture beam spectra are presented. Large amounts of single small-aperture beam data spectra can be collected using a spectrum analyzer, thereby avoiding the problem of a limited ensemble average encountered using the SH-WFS.

II. Jitter Measurements using Small-Aperture Single Beam

As described in Section 2.1.3, jitter measurements were made by transmitting a 1-2 mm diameter HeNe laser beam through the jet flow and directing it onto a lateral-effect detector. This single-beam measurement is equivalent to the measurement made by one subaperture of a SH-WFS. The advantage in using the lateral-effect detector is that spectra of the local slope can be computed to frequencies as high as 10 kHz (the frequency response of the UDT 301-DIV amplifiers) and with a very large number of ensemble averages, resulting in smooth spectra. A disadvantage of single beam small-aperture measurements is that the subaperture is somewhat larger than the subapertures of the SH-WFS, and consequently aperture averaging effects appear at lower wavenumbers. Three different types of small-aperture measurements were made during the investigation:

- Small-diameter single beam transmitting on the jet centerline;
- Small-diameter single beam transmitting off of the jet centerline (Y/D Translation);
- Small-diameter single beam translated through the jet centerline (Z/D Translation).
- Small-diameter single beam with a Z/D-translating control section (Control Section).

(i) Small-Aperture Jitter Spectra - Centerline Transmission

The jitter spectral development for both horizontal and vertical deflections are shown in Figs. 33 and 34, respectively. Both the horizontal and vertical jitter spectra show a power-law relationship by $X/D = 7$, which is in agreement with the findings for the mass-flux

spectral development shown in Fig. 19. The slopes for both the horizontal and vertical jitter signals are found to be different, with the slopes for the vertical jitter spectra equal to the expected Kolmogorov value of $-2/3$, while the slopes for the horizontal jitter spectra being closer to -1.

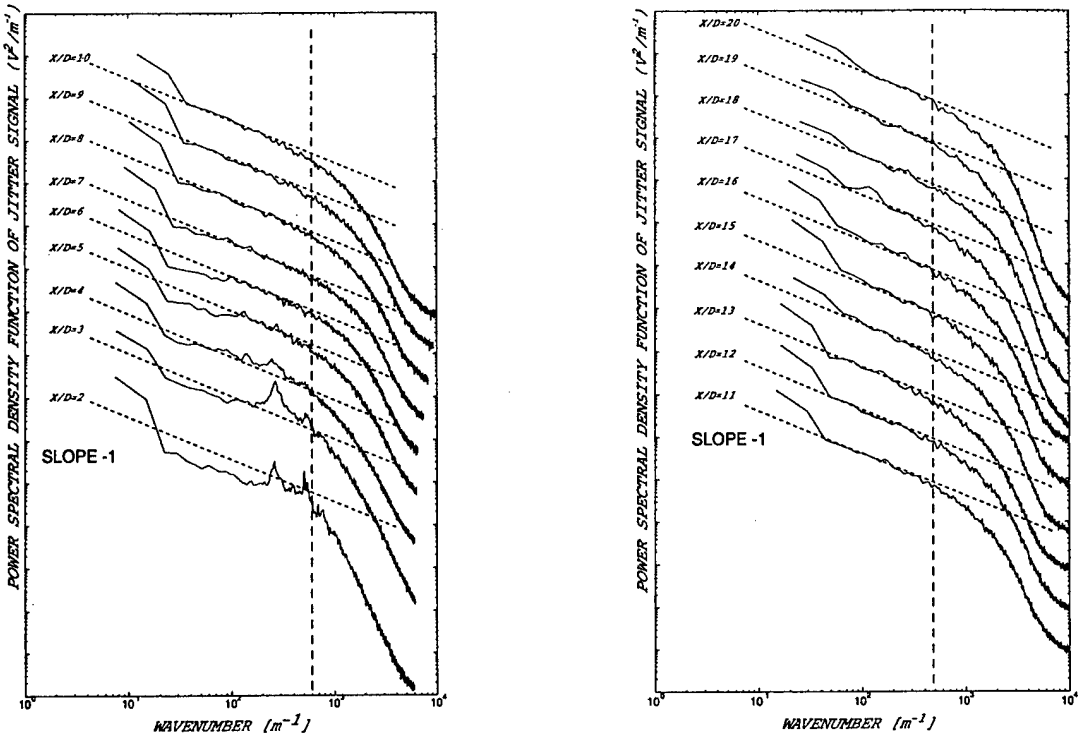

$X/D = 1 \rightarrow 10$ $\qquad$ $X/D = 11 \rightarrow 20$

Figure 33. Horizontal Jitter Spectral Development $X/D = 1 \rightarrow 20$

As with the mass flux spectra in Fig. 19, both the horizontal and vertical jitter spectra are seen to depart from a linear slope relation by $k \approx 500 \rightarrow 600$ for the horizontal jitter (Fig. 33) and by $k \approx 700$ for the vertical jitter (Fig. 34). This means that aperture averaging effects are taking place at spatial scales on the order of 1.5 mm, which is the approximate diameter of the small-aperture beam. The vertical jitter data in Fig. 34 was found to depart from its slope of -2/3 more consistently than the horizontal jitter data in Fig. 33.

The fact that the horizontal and vertical jitter spectra have differing slopes indicates non-Kolmogorov behavior in the optical statistics. An interesting correlation between fluid mechanic statistics and optical statistics is that longitudinal velocity spectra and vertical jitter spectra, having both been collected in the direction of maximum velocity, have the expected Kolmogorov slope values (-5/3 for velocity and -2/3 for jitter). The lateral velocity and horizontal jitter, on the other hand, having both been collected in the direction of minimum velocity have non-Kolmogorov spectral slopes of -4/3 and -1.

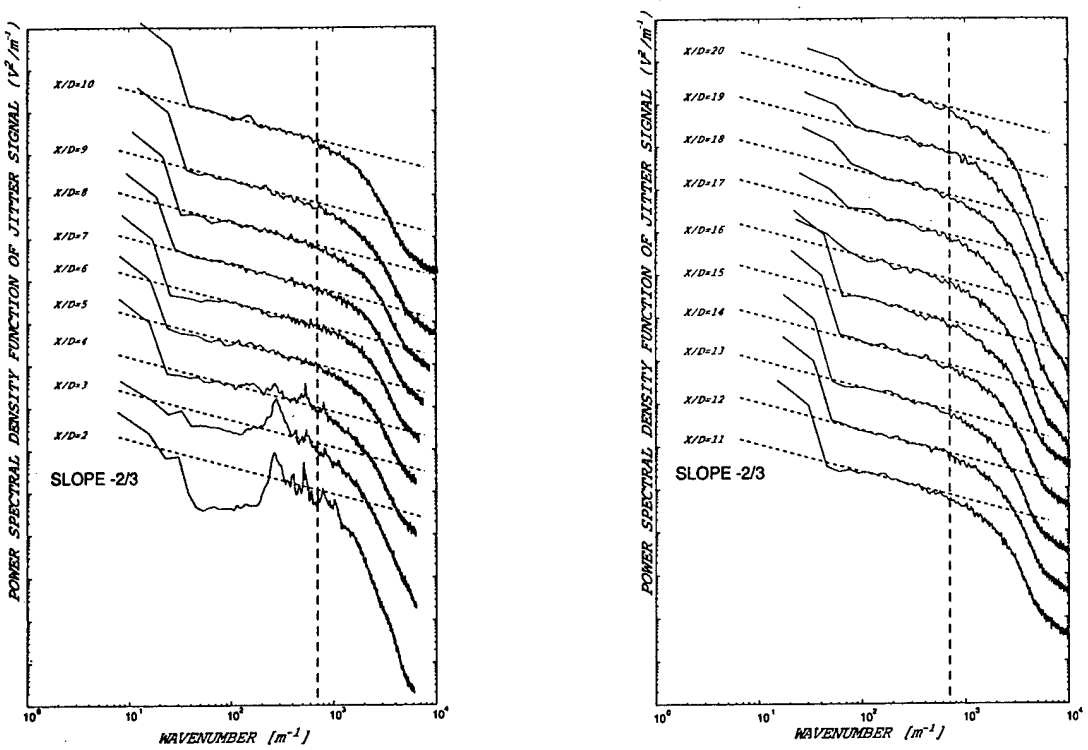

$X/D = 1 \rightarrow 10$ $X/D = 11 \rightarrow 20$

Figure 34. Vertical Jitter Spectral Development $X/D = 1 \rightarrow 20$

(a) Jet Flow Anisotropy

When discussing anisotropy in jet flows, self-similarity is an important concept. The Reynolds stresses were studied by Hussein et al.,[19] and as indicated in Fig. 35 show self-similar behavior. The profile for $< u_i u_j > /U_0^2(x)$ plotted against $r/r_{1/2}$ collapses for all streamwise directions beyond the development region. Important observations that can be concluded from this plot are that the Reynolds stresses exhibit significant anisotropy as revealed both in the shear stress and in the different normal stresses and that towards the jet's outer edge the Reynolds stresses decay with increasing $r/r_{1/2}$.

In most homogeneous turbulence experiments, however, turbulence is generated using a square-mesh biplane grid with round or square rods. The turbulence in these flows is homogeneous and quasi-isotropic in planes perpendicular to the streamwise direction. Experiment also proves that the component $< u_1^2 >$ is greater than $< u_2^2 >$ and $< u_3^2 >$, which are generally equal, so that the isotropy condition on the Reynolds stress tensor is not fulfilled.[19]

To balance the Reynolds stress, Comte-Bellot and Corrsin [20] improved the isotropy of the Reynolds stress tensor by using a small contraction located downstream of the grid. The contraction helped to reduce $< u_1^2 >$ to match it with $< u_2^2 >$ and $< u_3^2 >$. Uberoi[21]

concluded that in the absence of a mean velocity gradient, an originally anisotropic turbulence returns towards isotropy. The contraction changes the flow layout and provides more perturbation through the cross-stream direction. The energy supply required to maintain the structure of eddies in the inertial subrange is fulfilled, helping to explain why isotropy returns.

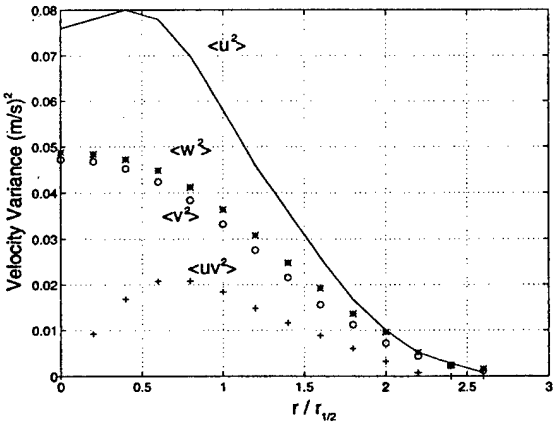

Figure 35. Profiles of Reynolds Stress
in the Self-Similar Round Jet - Hussein et al.

Referring to Fig. 35 for the case of the jet flow, in each of the levels above the jet exit self-similar behavior is exhibited. These fluctuations in the vertical and horizontal direction show strong anisotropy. Figure 36 presents horizontal and vertical angle-of-arrival spectra at level $X/D = 10$. In the vertical direction there is enough energy to maintain the inertial subrange. A lack of energy in the horizontal direction results in anisotropy.

This view is supported by our experimental results, which reveal differing slopes in the inertial subrange. The vertical signal shows Kolmogorov behavior with a spectral slope of -2/3, while the horizontal signal reveals non-Kolmogorov behavior with a slope of -1. When the horizontal signal is shifted up with respect to the vertical signal, as shown in the bottom part of Fig. 36, it is noted that the two curves become functionally similar. This functional similarity results due to aperture averaging effects that are dependent on the shape and diameter of the single beam alone and not on the orientation of the jitter.

(ii) Small-Aperture Jitter Spectra - Y/D-Translation

In order to investigate optical anisotropy for transmission through points off of the jet's centerline, a series of translation experiments were performed. While performing these experiments, a beam tube constructed from 0.32" OD and 0.2" ID acrylic tubing was used to shroud the beam as it transmitted through half of the jet flow in the Z-direction. Using the translating frame assembly shown in Fig. 5, it was possible to move the entire laser, beam tube, and detector assembly in the Y-direction. Y/D-Translation refers to the scenario where the beam tube is extended to the centerline of the jet, and the beam translated in the cross-stream (Y) direction.

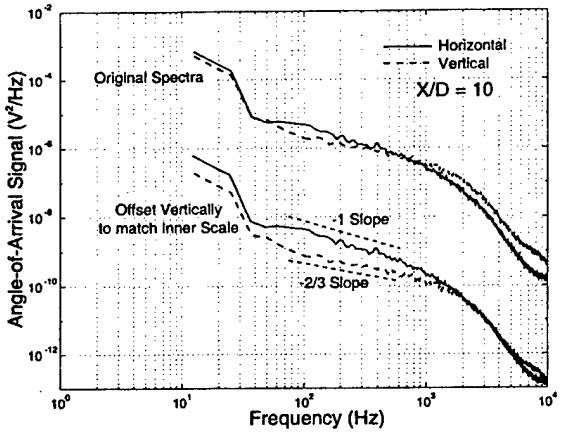

Figure 36. Aperture Averaging Region Comparison in Angle-of-Arrival Spectra

The presence of the beam tube extending to the jet centerline results in spectra being collected for transmission through only half of the jet flow. The effect of transmission through only half of the jet was investigated by collecting one spectra for transmission with the beam tube fully retracted, and a second spectra with the beam tube extended to the jet's centerline. The second spectra was multiplied by two under the assumption that transmission through only half of the jet would result in 50% of the full-jet energy. The full-jet and the doubled half-jet spectra are compared in Fig. 37, from which it can be seen that the doubled half-jet spectra is slightly less than the full-jet spectra, but functionally similar.

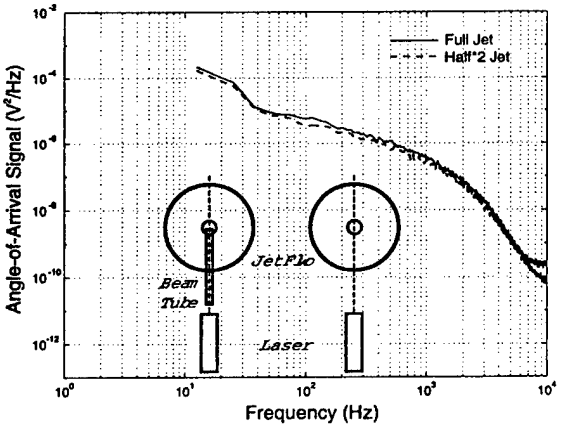

Figure 37. 2×Half- and Full-Jet Spectra

(a) Vertical Angle-of-Arrival Spectra - Y/D-Translation

Figure 38 shows the vertical angle-of-arrival spectra collected at $X/D = 10$ for Y/D-Translation. While collecting this data, the beam tube was extended to the centerline of the jet and the entire optical assembly translated from $Y/D = -2.5 \rightarrow 2.5$, as shown in Fig. 39.

Spectra collected near the centerline ($Y/D = 0$) reveal the strongest spectral energy, and show evidence of an inertial subrange that extends from 50 Hz to 1500 Hz with a $f^{-2/3}$ power-law relationship.

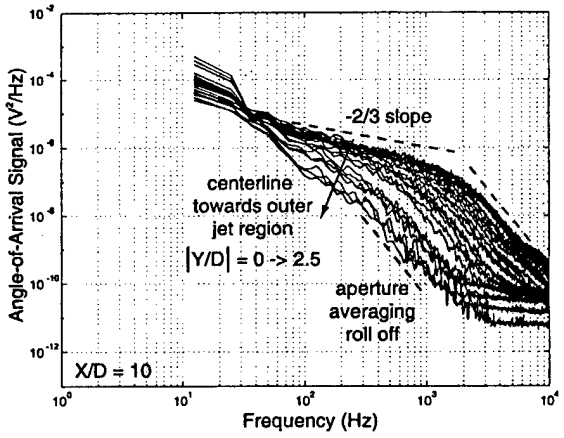

Figure 38. Vertical Angle-of-Arrival Spectra - Y/D-Translation

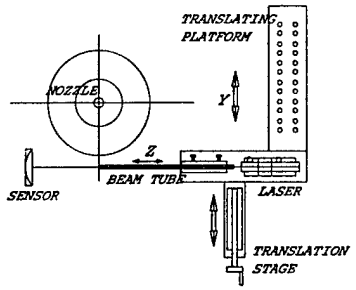

Figure 39. Y/D-Translation Configuration

As described earlier, the angle-of-arrival spectral slopes for Kolmogorov turbulence should follow a $f^{-2/3}$ power-law relationship. This is based on results of Rao et al.[17] where the wavefront phase temporal power spectrum was shown to follow a $f^{-8/3}$ power-law relationship. Using a relationship presented by Malley et al.,[18] the angle-of-arrival spectra can be shown to be related to the wavefront phase spectra multiplied by f^2. This results in a $-8/3 + 2 = -2/3$ power-law exponent for the angle-of-arrival spectra in Kolmogorov turbulence. Consequently, the spectra collected near the jet's centerline and shown in Fig. 38 exhibit the expected Kolmogorov turbulence statistics. Above 1500 Hz the spectral energy is noted to drop off at a higher rate due to aperture averaging effects.

In order to quantify spectral slopes, linear regression was performed on the angle-of-arrival spectra when plotted in log-log space. Performing a spectral fit in this manner requires care to ensure the fit is restricted to the inertial subrange, thereby avoiding erroneous spectral slopes that may result if the fit range is extended into either the outer scale or the aperature

averaging roll-off regions. Examining the spectra plotted in Fig. 38, it is noted that the strongest spectra exhibit an inertial subrange extending from 50 Hz to 1500 Hz. As the spectral energy decreases towards the edge of the jet, the frequency of the aperture averaging roll-off decreases from 1500 Hz at the jet's centerline to approximately 300 Hz in the outer-jet region. Consequently, it would be expected that a spectral fit range from 50 to 500 Hz would be sufficient to estimate spectral slopes across a significant portion of the jet, with only the outermost points susceptible to the effects of aperture averaging.

Figure 40 plots spectral slopes with cross-stream position for three different fit ranges. Fit ranges that extended up to 1000 Hz were found to encompass the aperture averaging roll-off region, consequently resulting in steeper slope estimates. An optimum fit range was found to be from 50 Hz to 600 Hz. The distribution of spectral slopes in Fig. 40 show the expected -2/3 Kolmogorov value at the center of the jet, with values decreasing towards the outer-jet region. More negative slopes towards the outer-jet region result from the aperture averaging region moving to lower frequencies ($\approx$ 300 Hz at $|Y/D| = 2.5$) and a decrease in overall spectral energy. As mentioned earlier, the inertial subrange is poorly defined in the outer-jet region making it difficult to fit spectral slopes in this region.

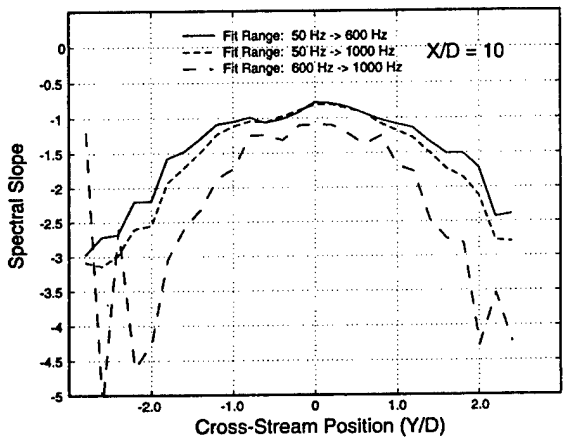

Figure 40. Vertical Angle-of-Arrival Spectral Slopes - Y/D-Translation

(b) Horizontal Angle-of-Arrival Spectra - Y/D-Translation

Figure 41 presents horizontal angle-of-arrival spectra with conditions identical to those presented earlier for vertical angle-of-arrival spectra. As before, spectra collected near the centerline ($Y/D = 0$) reveal the strongest spectral energy with an inertial subrange extending from 50 Hz to 1500 Hz. The power-law relationship for the horizontal angle-of-arrival spectra do not, however, exhibit the $f^{-2/3}$ behavior seen for vertical spectra but rather exhibit a f^{-1} behavior. This anisotropy of spectral slopes is indicative of non-Kolmogorov turbulence statistics. The origin of the anisotropy was discussed earlier, and is attributed to the large difference between the longitudinal and lateral mean velocities and the fact that the low lateral velocities make it difficult to maintain an inertial subrange.

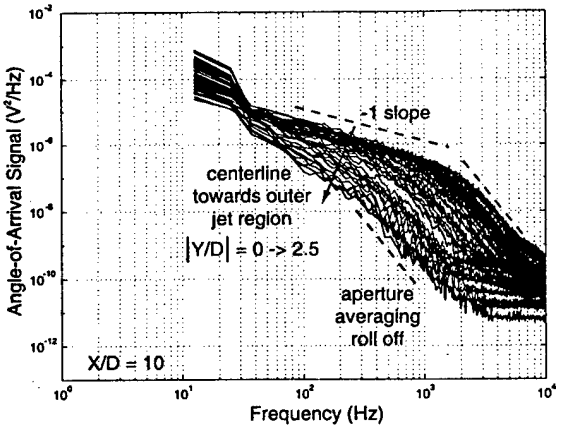

Figure 41. Horizontal Angle-of-Arrival Spectra - Y/D-Translation

Figure 42 plots the horizontal angle-of-arrival spectral slopes as a function of cross-stream position. Again as for the vertical signal, the spectral slopes decrease with cross-stream position due to reduced turbulence energy and the movement of the aperture averaging region to lower temporal frequencies.

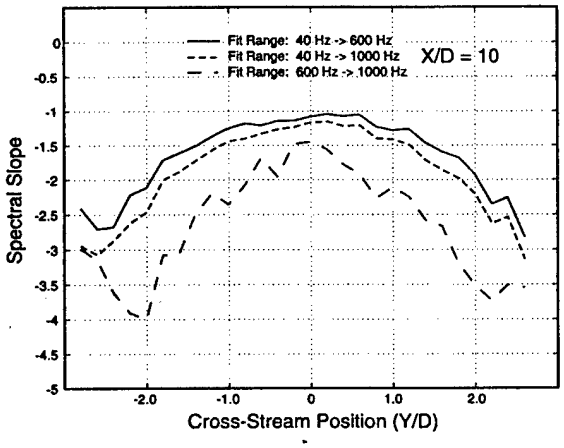

Figure 42. Horizontal Angle-of-Arrival Spectral Slopes - Y/D-Translation

The level of anisotropy in the jet can be estimated by taking the ratio of the horizontal-to-vertical spectral slopes. The resulting plot is shown in Fig. 43, from which it can be seen that the spectral slopes are most anisotropic at the centerline of the jet and that the anisotropy diminishes towards the outer-jet region. A reduction in anisotropy towards the outer jet region is most likely attributed to the longitudinal and lateral velocities becoming equal in the outer region.

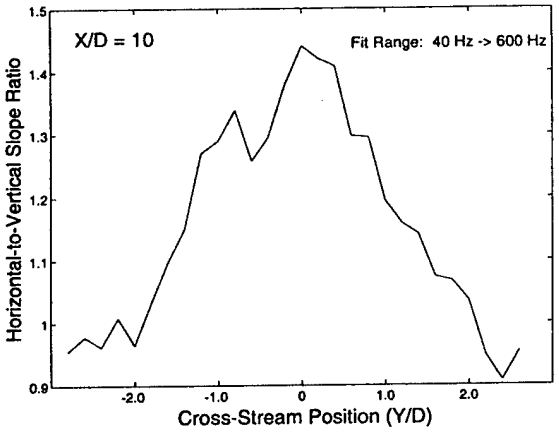

Figure 43. Horizontal-to-Vertical Spectral Slope Ratio - Y/D-Translation

(iii) Small-Aperture Jitter Spectra - Z/D-Translation

Z/D-Translation, illustrated in Fig. 44, refers to the scenario where the laser, directing mirrors, and lateral-effect detector are fixed with the beam transmitting through the jet at $Y/D = 0$. The beam tube is then moved in the Z-direction using a second translation stage (Item #6 in Fig. 1). The beam tube serves the purpose to protect the beam from optical aberrations through part of the jet, thereby enabling an investigation between varying the length of the aberrating optical path and beam degradation statistics.

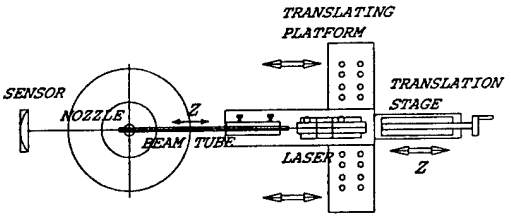

Figure 44. Z/D-Translation Configuration

Spectra of both the vertical and horizontal angle-of-arrival signals for Z/D-Translation are presented in Figs. 45 and 46, respectively. Again, as for Y/D-Translation, the vertical spectra show a $f^{-2/3}$ power-law relationship while the horizontal spectra show a f^{-1} relationship. The spectral spike at 120 Hz in the vertical spectra (Fig. 45) is attributed to electronic noise. The spike is most pronounced at the edge of the jet, and it was not evident for the vertical spectra collected under Y/D-Translation (Fig. 38). The noise spike is more pronounced for Z/D-Translation as the shortened aberrating path length reduces overall signal levels, making electronic noise more evident. A well defined inertial subrange and aperture averaging region are noted for spectra collected at $Z/D = 0$. The aperture averaging region decreases towards the outside of the jet as the turbulence strength decreases.

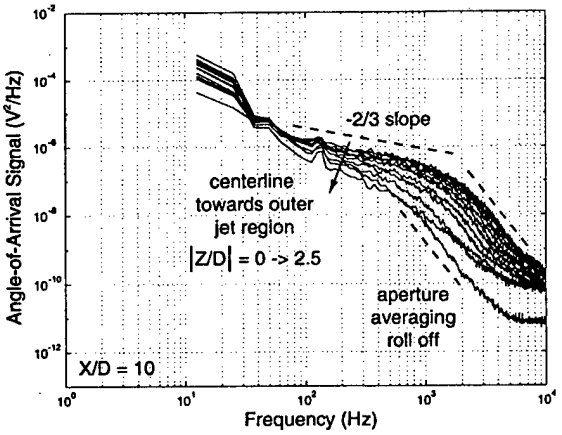

Figure 45. Vertical Angle-of-Arrival Spectra - Z/D-Translation

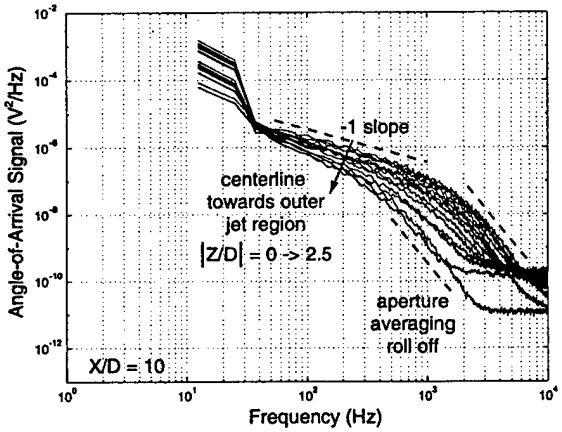

Figure 46. Horizontal Angle-of-Arrival Spectra - Z/D-Translation

Angle-of-arrival spectral slopes for Z/D-Translation shown in Fig. 47 again reveal anisotropy throughout the entire jet. The decline in spectral slope with Z/D is attributed to the fact that the inertial subrange decreases towards the outer-jet region, and consequently the fit range from 50 Hz to 600 Hz begins to fit points in the aperture averaging region, reducing spectral slopes.

(a) Angle-of-Arrival Variances

The angle-of-arrival variance is computed by integrating the area under the spectra of either the horizontal or vertical angle-of-arrival signals. The variance for Z/D-Translation is shown in Fig. 48, from which it can be seen that the log of the variance of the angle-of-arrival signal follows what appears to be a linear relationship with distance transmitted through the aberrating media. It is difficult to speculate how this relationship extrapolates to longer extended paths. It is expected that the variance of beam jitter should eventually saturate and become independent of path length. This does, however, also depend on the range of

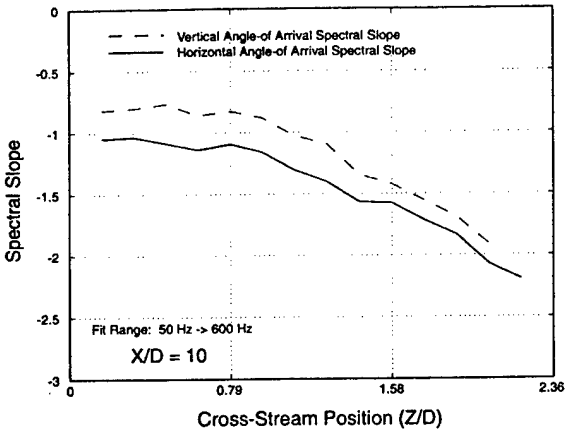

Figure 47. Angle-of-Arrival Spectral Slopes - Z/D-Translation

frequencies over which the variance is computed.

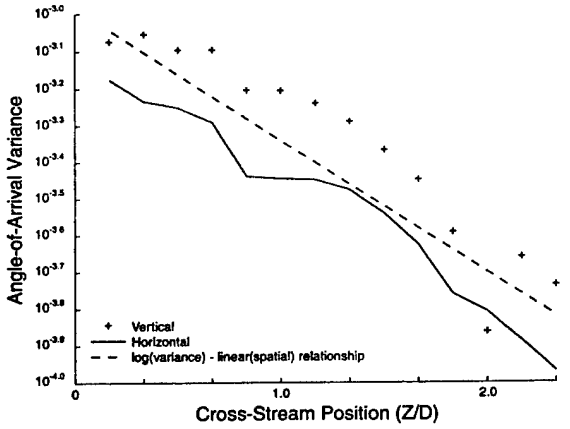

Figure 48. Vertical and Horizontal Variance: Z/D-Translation

The variance for Y/D-Translation is shown in Fig. 49. In this case, the beam transmits through half of the jet as the beam is translated with Y/D. The distance of aberrating media that the beam transmits through for this case is half of a circle (being that the jet flow is axisymmetric along the X-axis). Figure 48 indicates that the log of the variance of the signal has a linear relationship with distance, and consequently it can be hypothesized that the log of the variance for Y/D-Translation should resemble a semicircle. A semicircle has been overlayed over the data in Fig. 49, from which it can be seen that the data lies quite close to the semicircle. This reinforces the observation that the log of the variance of the angle-of-arrival signal is linearly related to the distance that the beam transmits through the aberrating media.

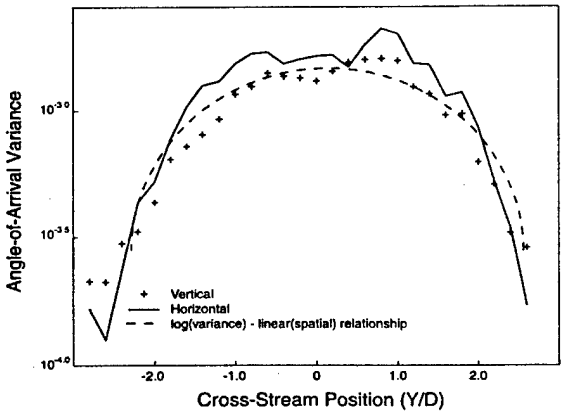

Figure 49. Vertical and Horizontal Variance: Y/D-Translation

(iv) Small-Aperture Jitter Spectra - Z/D-Translation with Control Section

Figures 50 and 51 show the angle-of-arrival spectra collected at $X/D = 10$ for beam displacement in the respective horizontal and vertical directions. While collecting this data, the control section between the two beam tubes was extended through the centerline of the jet and the entire optical assembly translated from $Z/D = -2.5 \rightarrow 2.5$, as shown in Fig. 5. The spectral spike located at 120 Hz in both directions is due to electronic noise and should be disregarded. This spectral spike was most pronounced for the Control Section measurements due to the relatively short aberrating path length, resulting in weak signal levels. Spectra collected near the center of the jet ($Z/D = 0$) reveal the strongest spectral energy, and show evidence of an inertial subrange that extends from 100 Hz to 1500 Hz with a $f^{-2/3}$ and f^{-1} power-law relationship. Conan et al.[22] show that the power spectra for angle-of-arrival spectra should follow a $f^{-11/3}$ power-law relationship in the inner scale region. This has been overlayed on both figures, from which it can be seen that the aperture averaging caused the spectra to roll off at a rate higher than $f^{-11/3}$.

Figures 52 and 53 present the respective horizontal and vertical angle-of-arrival spectra with conditions different from those presented earlier. This time the spectra were collected with the control section located at the jet's centerline ($Z/D = 0$) and the distance downstream of the jet's exit was increased ($X/D = 10 \rightarrow 20$). These plots reveal the strongest spectral energy with an inertial subrange extending from 100 Hz to 1500 Hz and once again the power-law relationship for the horizontal angle-of-arrival spectra was f^{-1} and the relationship for the vertical spectra $f^{-2/3}$. Anisotropy of spectral slopes is indicative of non-Kolmogorov turbulence statistics, as discussed earlier in the report.

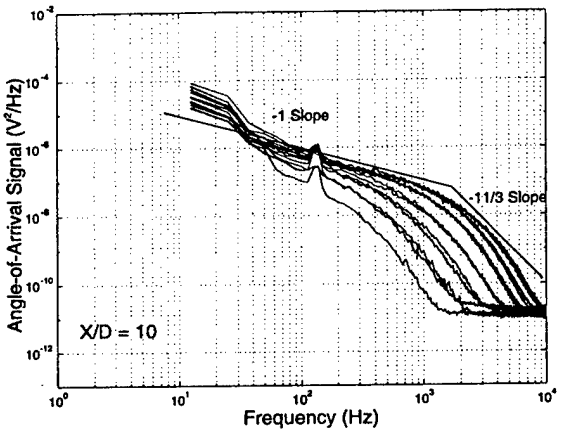

Figure 50. Horizontal Angle-of-Arrival Spectra - Z/D-Translation with Control Section

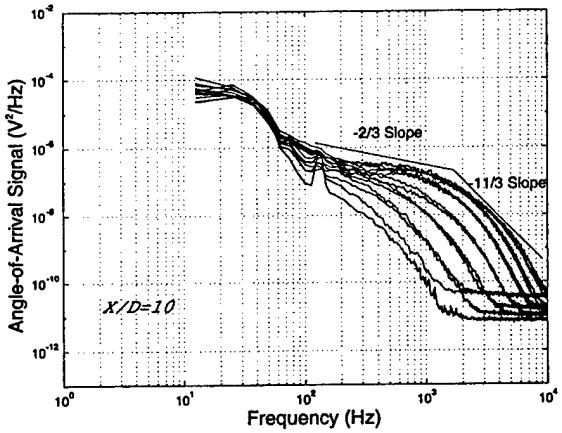

Figure 51. Vertical Angle-of-Arrival Spectra - Z/D-Translation with Control Section

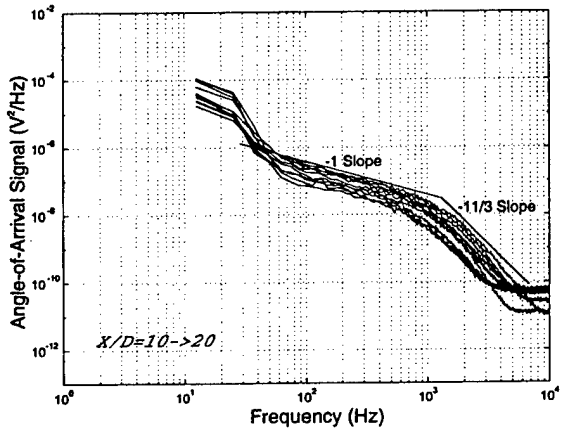

Figure 52. Horizontal Angle-of-Arrival Spectra - Z/D-Translation with Control Section

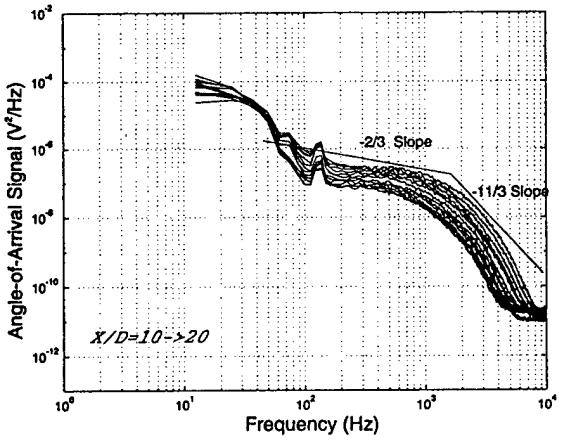

Figure 53. Vertical Angle-of-Arrival Spectra - Z/D-Translation with Control Section

3. CONCLUSIONS

The axisymmetric heated jet is a turbulent flow that is amenable to a wide variety of experimental measurements, permitting a detailed comparison between fluid-mechanic-based statistics and optical statistics. The research has compared fluid-mechanic statistics with optical statistics collected in the heated jet. Research has also been conducted examining statistics collected in regions of the jet flow that are know to have non-Kolmogorov behavior.

Both fluid-mechanic and optical-based statistics indicate anisotropy. Statistics collected in the direction of major flow are found to have Kolmogorov statistics, with an $f^{-5/3}$ power-law relationship in velocity fluctuations and an $f^{-2/3}$ power-law relationship in angle of arrival. Statistics collected in directions perpendicular to the mean flow direction were found to have non-Kolmogorov statistics, with an $f^{-4/3}$ power-law relationship in velocity fluctuations and an f^{-1} power-law relationship in angle of arrival.

Extending the results obtained in the heated jet to the scenario of **atmospheric transmission,** it can be hypothesized that vertical transmission would show less evidence of non-Kolmogorov statistics than horizontal transmission. During **vertical transmission,** angle-of-arrival statistics collected in the mean flow direction (East-West) would be Kolmogorov while angle-of-arrival statistics collected in a direction perpendicular to the mean flow direction (North-South) would appear non-Kolmogorov. During **horizontal transmission,** propagation coincident with the predominant wind vector would result in non-Kolmogorov statistics in both the horizontal and vertical angle-of-arrival statistics, while propagation normal to the mean wind vector would have Kolmogorov statistics in the horizontal angle-of-arrival signal and non-Kolmogorov statistics in the vertical angle-of-arrival signal.

4. PERSONNEL SUPPORTED

Post-Doctoral Assistant

Ming Xu
Post-Doctoral Research Assistant
Department of Mechanical and Manufacturing Engineering
University of Calgary

Research Assistants

Haibo Liu
Graduate Research Assistant #1
Department of Mechanical and Manufacturing Engineering
University of Calgary

Daniel Nugent
Undergraduate Research Assistant #1
Department of Mechanical and Manufacturing Engineering
University of Calgary

Neil McCann
Undergraduate Research Assistant #2
Department of Mechanical Engineering
Princeton University

Mirko Svigir
Undergraduate Research Assistant #3
Department of Mechanical and Manufacturing Engineering
University of Calgary

Roland Muwanga
Undergraduate Research Assistant #4
Department of Mechanical and Manufacturing Engineering
University of Calgary

Jason Bourgeois
Undergraduate Research Assistant #5
Department of Mechanical and Manufacturing Engineering
University of Calgary

Brendan McLean
Undergraduate Research Assistant #6
Department of Mechanical and Manufacturing Engineering
University of Calgary

5. PUBLICATIONS

6. INTERACTIONS / TRANSITIONS

6.1. Meeting Presentations

Liu, B., Hugo, R.J., Xu, M., "Optical and Velocity Turbulence Statistics in a Heated Axisymmetric Jet," AIAA-Paper Number 2003-3612, American Institute of Aeronautics and Astronautics, June 2003, Orlando FL.

Hugo, R.J., Liu, B., Xu, M., Eaton, F., "Angle-of-Arrival Spectral Slopes for Transmission through Non-Kolmogorov Turbulence," AIAA-Paper Number 2003-0681, American Institute of Aeronautics and Astronautics, January 2003, Reno NV.

Hugo, R.J., Liu, B., Xu, M., Eaton, F., "Optical Transmission and Turbulence Characteristics in a non-Kolmogorov Shear Flow," AIAA-Paper Number 2002-2271, American Institute of Aeronautics and Astronautics, May 2002, Maui HI.

Hugo, R.J., "Mechanical and Optical Turbulence Relationships in a Free-Shear Flow," AIAA-Paper Number 2001-2800, American Institute of Aeronautics and Astronautics, June 2001, Anaheim CA.

6.2. Consultative and advisory functions

6.3. Transitions

7. NEW DISCOVERIES

8. HONORS / AWARDS

REFERENCES

1. King, L. V., "On the convection of heat from small cylinders in a stream of fluid: determination of the convection constants of small platinum wires with applications to hot-wire anemometry," *Philos. Trans. Roy. Soc. London, Ser. A*, vol. 214, no. 14, pp. 373-432, Nov. 12, 1914.
2. Hugo, R.J., Nowlin, S.R., Eaton, F.D., Bishop, K.P., McCrae, K., "Hot-wire calibration in a Non-Isothermal Incompressible Pressure Variant Flow," in, Airborne Laser Advanced Technology II. eds. T.D. Steiner and P.H. Merritt, SPIE - International Society of Optical Engineering, Vol. 3706, pp. 11-22, April 1999.
3. Willmarth, W.W., Bogar, T.J., "Survey and new measurements of turbulent structure near the wall," *Physics of Fluids,* 20, S9-S21, 1977.
4. Lueptow, R.M., Breuer, K.S., Haritonidis, J.H., "Computer-aided calibration of X-probes using a look-up table," *Experiments in Fluids,* 6, pp. 115-118, 1988.
5. Bruun, H.H., *Hot-Wire Anemometry, Principles and Signal Analysis*, pp. 55-57, Oxford University Press, 1995.
6. Hugo, R.J., and Jumper, E.J., "Applicability of the Aero-Optic Linking Equation to a Highly Coherent, Transitional Shear Layer," *Applied Optics,* pp. 4392-4401, vol. 39, no. 24, 2000.
7. Malacara, D., *Optical Shop Testing,* John Wiley and Sons, New York, 1978.
8. McMackin, L., Masson, B., Clark, N., Bishop, K., Pierson, R., and Chen, E., "Hartmann wave front sensor studies of dynamic organized structure in flowfields," *AIAA Journal,* pp. 2158-2164, Vol. 33, No. 11, November 1995.
9. Huang, L.-S. and Ho, C.-H., "Small-Scale Transition in a Plane Mixing Layer," Journal of Fluid Mechanics, vol. 210, pp. 475-500, 1990.
10. Mathieu, J. and Scott, J., 2000, *An Introduction to Turbulent Flow*, Cambridge University Press, 374 pp.
11. Wyngaard, J. C., Izumi, Y., and Collins, S.A., "Behavior of the Refractive Index Structure Parameter Near the Ground," *Journal of the Optical Society of America*, pp. 1646-1650, Vol. 61, 1971.
12. Kaimal, J. C., "Turbulent Spectra, Length Scales and Structure Parameters in the Stable Surface Layer," *Boundary-Layer Meteorology*, pp. 289-309, Vol. 4, 1973.
13. Dayton, D., Pierson, B., Spielbusch, B., and Gonglewski, J., "Atmospheric structure function measurements with a Shack-Hartmann wave-front sensor," *Optics Letters,* Vol. 17, No. 24, pp. 1737-1739, 1992.
14. Nicholls, T., Boreman, G., and Dainty, J., "Use of a Shack-Hartmann wave-front sensor to measure deviations from a Kolmogorov phase spectrum," *Optics Letters,* Vol. 20, No. 24, pp. 2460-2462, 1995.
15. Rao, C., Jiang, W., and Ling, N., "Measuring the power-law exponent of an atmospheric turbulence phase power spectrum with a Shack-Hartmann wave-front sensor," *Optics Letters,* Vol. 24, No. 15, pp. 1008-1010, 1999.
16. Rao, C., Jiang, W., and Ling, N., "Atmospheric parameters measurements for non-Kolmogorov turbulence with Shack-Hartmann wavefront sensor," *Proc. SPIE* 3763, pp. 84-91, 1999.
17. Rao, C., Jiang, W., and Ling, N., "Atmospheric characterization with Shack-Hartmann wavefront sensors for non-Kolmogorov turbulence," *Optical Engineering,* Vol. 41, No. 2, pp. 534-541, 2002.

18. Malley, M.M., Sutton, G.W., and Kincheloe, N., "Beam-jitter measurements of turbulent aero-optical path differences," *Applied Optics,* pp. 4440-4443, Vol. 31, No. 22, August 1992.
19. Hussein, H. J., Capp, S. and George, W.K., "Velocity measurements in a high-Reynolds-number, momentum-conserving, axisymmetric, turbulent jet," *Journal of Fluid Mechanics,* vol. 258, pp. 31-75, 1994.
20. Comte-Bellot, G., Corrsin, S., "The use of a contraction to improve the isotropy of grid generated turbulence," *Journal of Fluid Mechanics,* vol. 25, pp. 657-682, 1966.
21. Uberoi, M.S. "Effect of wind-tunnel contraction on free-stream turbulence," *Journal of Aerospace Sciences,* Vol. 23, pp. 754-764, 1956.
22. Conan, J.M., Madec, P.Y., Rousset, G., "Real Time and Post-Fact Solar Image Correction," 13th Sacramento Peak Summer Workshop, 1992.